

การจำลองปรากฏการณ์ทางฟิสิกส์ในนิวตรอนมอนิเตอร์ของสถานีตรวจวัดนิวตรอนสิรินธร



นาย คณิน อึ้งสกุลศิริ

สถาบันวิทยบริการ

จุฬาลงกรณ์มหาวิทยาลัย

วิทยานิพนธ์นี้เป็นส่วนหนึ่งของการศึกษาตามหลักสูตรปริญญาวิทยาศาสตรมหาบัณฑิต

สาขาวิชาฟิสิกส์ ภาควิชาฟิสิกส์

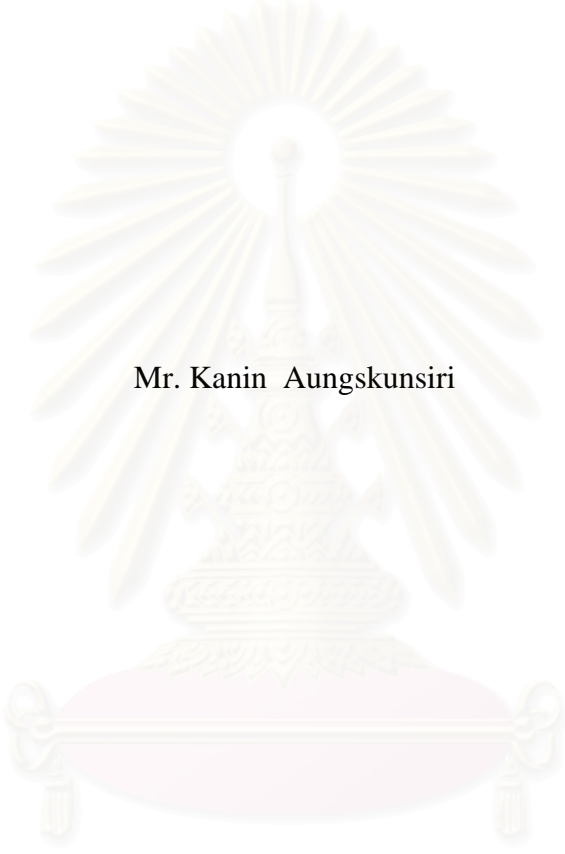
คณะวิทยาศาสตร์ จุฬาลงกรณ์มหาวิทยาลัย

ปีการศึกษา 2547

ISBN 974-17-6699-8

ลิขสิทธิ์ของจุฬาลงกรณ์มหาวิทยาลัย

SIMULATION OF PHYSICAL PHENOMENA IN THE NEUTRON MONITOR
OF THE PRINCESS SIRINDHORN NEUTRON MONITOR



Mr. Kanin Aungskunsiri

สถาบันวิทยบริการ
จุฬาลงกรณ์มหาวิทยาลัย

A Thesis Submitted in Partial Fulfillment of the Requirements
for the Degree of Master of Science in Physics

Department of Physics
Faculty of Science
Chulalongkorn University
Academic Year 2004
ISBN 974-17-6699-8

Thesis Title Simulation of Physical Phenomena in the Neutron Monitor of
the Princess Sirindhorn Neutron Monitor
By Mr. Kanin Aungskunsiri
Field of Study Physics
Thesis Advisor Burin Asavapibhop, Ph.D.
Thesis Co-advisor Associate Professor David Ruffolo, Ph.D.

Accepted by the Faculty of Science, Chulalongkorn University in Partial Fulfillment
of the Requirements for the Master's Degree

..... Dean of the Faculty of Science
(Professor Piamsak Menasveta, Ph.D.)

THESIS COMMITTEE

..... Chairman
(Associate Professor Mayuree Natenapit, Ph.D.)

..... Thesis Advisor
(Burin Asavapibhop, Ph.D.)

..... Thesis Co-advisor
(Associate Professor David Ruffolo, Ph.D.)

..... Member
(Assistant Professor Rattachat Mongkolnavin, Ph.D.)

..... Member
(Rujikorn Dhanawittayapol, Ph.D.)

คณิน อึ้งสกุลศิริ: การจำลองปรากฏการณ์ทางฟิสิกส์ในนิวตรอนมอนิเตอร์ของสถานี
 ตรวจวัดนิวตรอนสิรินธร. (SIMULATION OF PHYSICAL PHENOMENA IN THE
 NEUTRON MONITOR OF THE PRINCESS SIRINDHORN NEUTRON MONITOR)
 อ. ที่ปรึกษา: อ.ดร. บุรินทร์ อัสวพิภพ, อ. ที่ปรึกษาร่วม: รศ.ดร. เดวิด รุฟโฟโล 107 หน้า.
 ISBN 974-17-6699-8.

นิวตรอนมอนิเตอร์เป็นอุปกรณ์ที่ใช้ในการตรวจวัดรังสีคอสมิกนิวตรอน การตรวจวัด
 นิวตรอนเป็นประโยชน์ในการศึกษาปรากฏการณ์ทางฟิสิกส์ในอวกาศ อัตราการวัดนิวตรอนถูก
 นำไปใช้ในการคาดการณ์ล่วงหน้าเกี่ยวกับการเข้ามาของรังสีคอสมิกที่มีพลังงานสูง ซึ่งสามารถ
 ส่งผลกระทบต่ออย่างรุนแรงต่อเทคโนโลยีของเรา ในวิทยานิพนธ์นี้ ได้ทำการศึกษาเกี่ยวกับ
 ปรากฏการณ์ทางฟิสิกส์ในเครื่องตรวจวัดนิวตรอน โดยใช้โครงสร้างที่จำลองขึ้นมาจากเครื่อง
 ตรวจวัดนิวตรอนสิรินธร โดยการศึกษาทางคอมพิวเตอร์ด้วยโปรแกรม GEANT4 หน้าทีของ
 องค์ประกอบหลักในเครื่องนิวตรอนมอนิเตอร์โดยการจำลองได้ถูกนำมาพิจารณา จากการจำลอง
 ได้ผลที่สอดคล้องกับแนวคิดทางทฤษฎี การศึกษาได้พิจารณานิวตรอนที่ถูกกระเจิงจากน้ำบน
 พื้นดิน นอกจากนี้การจำลองยังได้แสดงให้เห็นถึงผลของอนุภาคประจุชนิดอื่นที่เข้าสู่เครื่อง
 ตรวจวัดนิวตรอน นอกเหนือไปจากอนุภาคนิวตรอน

สถาบันวิทยบริการ จุฬาลงกรณ์มหาวิทยาลัย

ภาควิชา ฟิสิกส์
 สาขาวิชา ฟิสิกส์
 ปีการศึกษา 2547

ลายมือชื่อนิสิต
 ลายมือชื่ออาจารย์ที่ปรึกษา
 ลายมือชื่ออาจารย์ที่ปรึกษาร่วม

4572234023: MAJOR PHYSICS

KEY WORD: Neutron Monitor / neutron / cosmic rays / Princess Sirindhorn / GEANT4

KANIN AUNGSKUNSIRI: SIMULATION OF PHYSICAL PHENOMENA IN THE NEUTRON MONITOR OF THE PRINCESS SIRINDHORN NEUTRON MONITOR.

THESIS ADVISOR: BURIN ASAVAPIBHOP, PH.D., THESIS CO-ADVISOR: ASSOCIATED PROFESSOR DAVID RUFFOLO, PH.D., 107 pp. ISBN 974-17-6699-8.

Neutron Monitors are devices for detecting cosmic ray neutrons. The detection of neutrons allows us to study the astrophysical phenomena in the outer space. The neutron counting rates are used to predict the arrival of high energy primary cosmic rays, which cause many serious effects to our technologies. In this thesis, a study has been carried out to investigate the physics phenomena in the neutron monitor using geometry modeled from the Princess Sirindhorn Neutron Monitor. The functions of the main neutron monitor's components have been determined by computer simulation using GEANT4 program. The simulations provided results which are in agreement with the theoretical considerations. The effects of scattered neutrons from water on the ground have been determined. The simulations also indicated the contribution of charged particles arriving into the detector besides neutrons.

สถาบันวิทยบริการ
จุฬาลงกรณ์มหาวิทยาลัย

Department Physics

Field of study Physics

Academic year 2004

Student's signature

Advisor's signature

Co-advisor's signature

Acknowledgements

This thesis is partially supported by the Basic Research Grant from the Chulalongkorn University Research Unit and the Thailand Research Fund. I wish to sincerely thank for their funding. Thanks to everyone in High Energy Physics Research Group and in Space Physics and Energetic Particles Research Group for their help and advice with great friendliness. Thanks to the committee for checking my report and inspecting on my work. Thanks also to friends in Physics Department for their friendship and sincerely express my special thanks to Dr. Burin Asavapibhop, my advisor; and Assoc.Prof.Dr. David Ruffolo, my co-advisor; for their encouragement, attention, and valuable guidance that is one reason for successful in this work. Finally, I would like to give credit for the success of this work to my mother and family at Phuket, who always support me with great intention and always be there when I need it.



สถาบันวิทยบริการ
จุฬาลงกรณ์มหาวิทยาลัย

Table of Contents

Abstract (Thai)	iv
Abstract (English)	v
Acknowledgements	vi
Table of Contents	vii
List of Tables	ix
List of Figures	x
1. Introduction	1
1.1 Introduction	1
1.2 Objectives	2
1.3 Outline of This Thesis	2
1.4 The Usefulness of This Thesis	3
2. Theoretical Background	4
2.1 Cosmic Rays	4
2.2 Earth's Magnetosphere and Cutoff Rigidity	7
2.3 Cosmic Rays in the Atmosphere	11
2.3.1 Neutrons	12
2.4 Space Weather	14
2.4.1 Solar Activities	15
2.4.2 Effects on Everyday Life of Humans	17
3. Neutron Physics and Neutron Detection	23
3.1 The Discovery of the Neutron	23
3.2 Neutron Sources	24
3.3 Neutron Attenuation	26
3.4 Slow Neutron Detection	34
3.5 The Proportional Counter	37

4. The Neutron Monitor	39
4.1 Timeline of Early Discovery	39
4.2 The Neutron Monitor Design	40
4.2.1 The IGY Monitor	40
4.2.2 The NM64 Monitor	43
4.2.3 The Princess Sirindhorn Neutron Monitor	45
5. GEANT4	47
5.1 The <i>main()</i> method	47
5.2 User Initialization and Action Class	51
5.3 Detector Geometry	54
5.4 Particles and Physics Processes	59
5.5 Run and Event	62
5.6 Physics List Package	64
6. Simulations, Results and Discussions	65
6.1 The Working Procedure	65
6.2 The Geometry	67
6.3 The Proportional Counter	69
6.4 Counts in the Neutron Monitor	79
6.5 The Lead Producer	85
6.6 The Inner Moderator	88
6.7 The Reflector	91
6.8 Effects from Environments	93
6.9 Neutron Monitor as a Cosmic Ray Detector	95
7. Conclusions	100
References	102
Appendix	105
Curriculum Vitae	107

List of Tables

	Page
Table 3.1 Scattering properties of several nuclei.....	33
Table 4.1 Comparison between Standard IGY Monitors and NM64 Monitors.....	41
Table 4.2 Neutron Counters used in IGY and NM64 monitors.....	42
Table 4.3 Specification of the Princess Sirindhorn Neutron Monitor.....	46
Table 6.1 Differences parameter from specification and used in the simulations.....	68
Table 6.2 The stopping path length in BF_3 chamber.....	74
Table 6.3 Comparison between theory and simulation.....	76
Table 6.4 An example of determination of total counts and detection efficiency for 5 incoming neutrons.....	80
Table 6.5 Neutron interaction in lead at various energy.....	86
Table 6.6 Comparison between the use of moderator thickness.....	89

List of Figures

	Page
Figure 2.1 Charge spectrum of the cosmic rays, from $Z=1$ through $Z=28$, as observed at the Earth (solid line), compared to the general solar system abundances; dashed line.....	4
Figure 2.2 Victor Hess, discoverer of the cosmic rays after his 1912 balloon flight that reached an altitude of 47,500 feet.....	5
Figure 2.3 Cosmic ray shower diagram.....	7
Figure 2.4 The Earth's magnetosphere.....	8
Figure 2.5 A simulated cosmic ray orbit, representing the effect of the Earth's magnetic field on incoming charged particles.....	9
Figure 2.6 Cosmic ray neutron monitors around the world in 1997 and vertical cutoff rigidity map.	10
Figure 2.7 Spectrum of the average differential neutron flux in the atmosphere at 40,000 ft. and 45° latitude based on the measurements of NASA-Ames and normalized to a 1-10 MeV neutron flux of $0.85 \text{ n/cm}^2 \text{ sec}$	12
Figure 2.8 The 1-10 MeV atmospheric neutron flux as a function of altitude base on aircraft and balloon measurements.	13
Figure 2.9 The 1-10 MeV neutron flux as a function of geographical latitude based on aircraft neutron measurements.	14
Figure 2.10 The general Sun's structure (left), and sunspots on the surface (right).	15
Figure 2.11 Solar Activities.	16
Figure 2.12 The coronal mass ejection.....	18

Figure 2.13	A variety of effects from Space Weather phenomena.	19
Figure 2.14	Effects on power systems.	20
Figure 3.1	James Chadwick.	24
Figure 3.2	Elastic scattering kinematics for an incident particle of mass m , initial energy, E_0 and speed v_0 , colliding with a particle of mass M in (a) the laboratory and (b) the center-of-mass frames of reference.	27
Figure 3.3	Considering the probability of the scattering neutron (in cm frame) between the scattering angle θ and $\theta + d\theta$. Note that \vec{r} is a radius vector rotating from $\theta = 0^\circ$ to $\theta = 180^\circ$, and from $\phi = 0^\circ$ to $\phi = 360^\circ$	29
Figure 3.4	Probability distribution for neutrons (with initial energy E_0) having a final energy E_1 after being elastic scattering by a stationary target with mass number A	30
Figure 3.5	Energy dependence of cross sections for neutron absorptions on ^3He , ^6Li and ^{10}B and for total scattering by ^1H	35
Figure 3.6	The geometry of a filled-gas proportional counter.	37
Figure 4.1	A standard 12-counter IGY neutron monitor.	40
Figure 4.2	A 6-NM64 monitor [Carmichael (1964)].	44
Figure 4.3	General geometry of NM64 monitors.	45
Figure 6.1	The working procedure.	66
Figure 6.2	A 3-Tube NM64 geometry.	68
Figure 6.3	Neutron capture events in a BF_3 proportional chamber.	69
Figure 6.4	Energy distribution produced by a neutron source in a PB-28 Chalk River Neutron Counter. The plot is acquired from the <i>NM-64 Neutron Monitor Specification Data Sheet</i>	71

- Figure 6.5 Energy spectrum from signal probes of a bare BP-28 counter (which will be set up for the Princess Sirindhorn Neutron Monitor). The counts have been collected for a period of about 15 days in 2004 at Chulalongkorn University. (Courtesy of Alejandro Saiz.) 71
- Figure 6.6 Energy spectrum from four selected counters in the Newark Neutron Monitor at Australia. 72
- Figure 6.7 Energy distribution from a BF_3 neutron counter. Figures in the left panel display distribution in linear scale while the right panel are the same plot in logarithmic scale. The gas density in the BF_3 tube is (a,b) 0.1 kg/m^3 , (c,d) 0.68 kg/m^3 , and (e,f) 2.0 kg/m^3 . Note that the wall effect decreases while the effect from the Compton scattering expands widely. This is because of the higher grammage (or density of the medium) in the detector. 75
- Figure 6.8 Energy deposit in the BF_3 gas chamber from electrons produced by the Compton scattering of a 0.48-MeV gamma (left), and (right) the plots of Compton scattering probabilities versus grammage..... 76
- Figure 6.9 The simulation schematic. Incoming neutrons with various initial energies were shot vertically and randomly in position on the top of the Neutron Monitor..... 77
- Figure 6.10 Deposited energy in the BF_3 gas chamber with density 0.68 kg/m^3 . A million neutrons were shot vertically and randomly on the top surface of the 9-Tube NM64. The initial kinetic energy of the neutron are (a) 0.025 eV, (b) 2 MeV, and (c) 100 MeV. The bin size of the histograms is 0.05 MeV/bin. 78
- Figure 6.11 Total counts and detection efficiency. A flux of 10^5 neutrons were initiated vertically on the top of the 9Tubes-NM with various kinetic energies from 0.025 eV to 10 GeV. Note that the incident neutron beam was randomized on the top plain of the detector. The grammage parameter 0.68 kg/m^3 and 100 kg/m^3 were applied. The last graph is the comparison of the total counts and detection efficiency at grammage parameter 100 kg/m^3 81

Figure 6.12	Total counts and detection efficiency from three different number of counters; 1, 9, and 19 counters.....	83
Figure 6.13	Total counts Ratio for the use of 1,2,3,6, and 9 counters in the detector. The values are the ratio of the use of a single counter. Note that the incoming neutrons were initiated in the vertical direction.	84
Figure 6.14	Total counts and detection efficiency, at various incoming neutron energies, from a 9-Tube NM64 without a lead producer compared with the polyethylene replacement and a general geometry using lead producer.	87
Figure 6.15	Total counts ratio and detection efficiency ratio at various incoming neutron energies between the geometry with moderator implemented and the geometry without moderator.....	90
Figure 6.16	Percentages of reflecting neutrons from the reflector with a thickness of 3 inches.....	92
Figure 6.17	Neutron reflection from surroundings.....	93
Figure 6.18	Simulation schematic. Neutrons were initiated obliquely with the angle 45° on the water. The reflector made of low density polyethylene with a thickness of 3 inches are placed at the distance of 22 cm from the position of the incident neutrons. Note that the height of the water and the concrete were set to 1 cm and 10 cm, respectively.....	94
Figure 6.19	Reflected neutrons from the ground to the reflector (solid line), and which is traveling through the reflector (dotted line). The black lines (c and f) are from the consideration of having only water, and the blue lines (b and e) are from the case of having only concrete, and the red lines (a and d) are from the case of having water above the concrete.	95
Figure 6.20	Detection efficiency of a NM-64 with $^{10}\text{BF}_3$ courters for 6 different particle species arriving in the vertical incident direction. This result was determined using FLUKA combined with programs written by Clem. [Clem et al. (2000)]	97
Figure 6.21	Total neutron counts in a 9-Tube NM64 from the arrival of six different species of particles; π^+ , π^- , μ^+ , μ^- , p, and n.	97

Chapter 1

Introduction

1.1 Introduction

The sky is not nearly as benign as we might think, even with respect to the cosmic ray shower in the atmosphere. Therefore, the atmospheric environment is the result from high-energy cosmic rays traveling in every direction through the Earth's magnetosphere, striking air molecules, and generating a cascade of several particles showering toward the ground.

Cosmic rays are termed for energetic particles coming from outer space. They are produced from objects such as neutron stars, black hole etc. The Sun is the primary source for cosmic rays entering the Earth. Therefore, the effects of solar cosmic rays on the Earth are the results from activities on the Sun's surface. Moreover, there are other kinds of cosmic rays which are believed to come from outer solar system. These kinds of cosmic rays are lower in abundances, but much more energetic.

Monitoring cosmic ray is one way to investigate the activities on the Sun's surface and other phenomena in the galaxy. Scientists setup neutron monitor stations in order to detect neutrons from the sky. These neutrons are produced in the atmosphere from the cosmic ray showers. The neutron counts in the detector are the indicators for the flux of the entering cosmic rays, which is related to the astrophysical phenomena in the space.

In our daily life, monitoring cosmic rays is important since the cosmic rays affects us both direct and indirect ways. Cosmic rays can cause many problems from low to serious level. We would predict the entering of primary cosmic rays by monitoring the neutrons. This is useful because we can prevent or reduce

damage from their anomaly incoming.

In this thesis, we simulate the physics phenomena in the neutron monitor using geometry obtained from the Princess Sirindhorn Neutron Monitor. The goal is to determine the aspect of counts in the detector as we acquire from the theory and measurement. Furthermore, we want to determine the function of the material used in the geometry. The neutron counts from various incoming neutron energies are determined. In addition, the effects of other incoming charged particles, which can contribute to neutron counts in the detector, are considered.

1.2 Objectives

The objectives of this work are as follows:

- Simulate the neutron counts from the neutron monitor using geometry obtained from the Princess Sirindhorn Neutron Monitor.
- Simulate the energy distribution in the neutron counter and compare the simulation results with the theory and the preliminary measurement.
- Determine the function of the neutron monitor's components.
- Simulate the contribution from other atmospheric charge particles to the total neutron counts.

1.3 Outline of This Thesis

We start with chapter 1 by introducing the concept of this thesis, indicating the objectives, and defining the usefulness of this thesis. Next, in chapter 2, we present some basic knowledge about cosmic rays, Earth's magnetosphere and cutoff rigidity, cosmic rays in the atmosphere, and space weather; which affects our everyday life. In chapter 3, we present the neutron physics and theoretical consideration on neutron detections which facilitate us to understand the physics process in the neutron monitor. Chapter 4 illustrates the neutron monitor which has been classified into two prototypes; the IGY and NM64 neutron monitors.

Chapter 5 is about GEANT4 which is the key software used in our work. In this chapter, we introduce principal concepts of the general program and provide a description of the principle routines implemented in the main program. In chapter 6, we present the simulations and results. The result for each simulation is discussed. Chapter 7 is the last chapter stating the conclusion for all of the simulations in this thesis.

1.4 The Usefulness of This Thesis

The usefulness of this project is as follows:

1. We have obtained the energy distribution which indicated the neutron capture event in the BF_3 proportional counters. The results are compared with theory and preliminary measurements.

2. We have obtained the total counts and the detection efficiency of the neutron monitor for specific incoming neutron energies. These results cannot be acquired from the observation, but are particularly achieved from the simulations.

3. We have determined the function of the neutron monitor's components. The results are useful for comparing with the experimental measurements.

4. We have simulated the response of the neutron monitor to the atmospheric charge particles. The results indicate the contribution of other incoming charge particles to the neutron counts which can only be studied in the simulation. The results allow us to use the neutron monitor to detect charged particles besides neutrons.

Chapter 2

Theoretical Background

2.1 Cosmic Rays

Energetic particles that are found in space and filtered through our atmosphere are called cosmic rays. The cosmic ray abundance is shown in Figure 2.1. Protons, nucleus of hydrogen atoms, are the most portions with a fraction of 90% that can be found in space. Alpha particle comes second with a

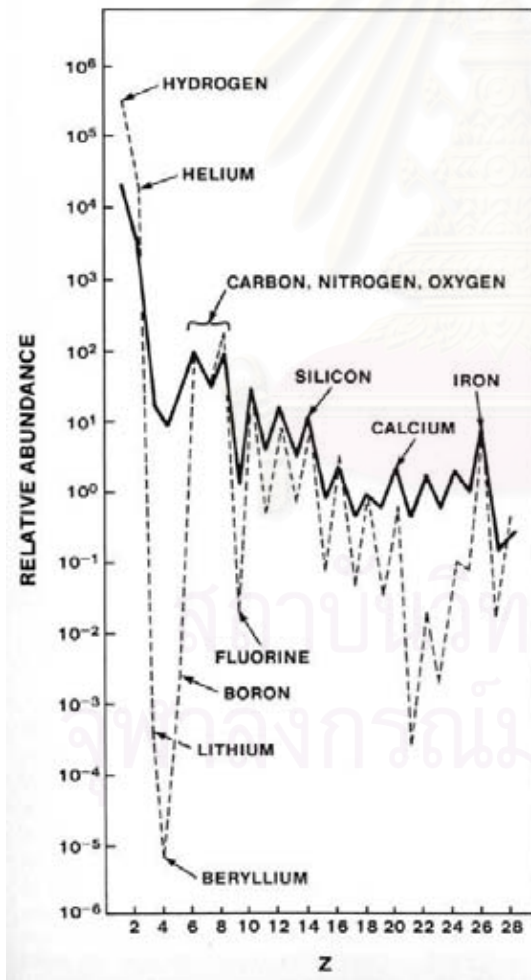


Figure 2.1: Charge spectrum of the cosmic rays, from $Z=1$ through $Z=28$, as observed at the Earth (solid line), compared to the general solar system abundances; dashed line. (Source: **Friedlander, Michael W.**, *Cosmic Rays*, 1989, page 65.)

fraction of about 9%, and another 0.01% is nuclei of other atom. In addition, gamma rays from outer space are also called cosmic rays.



Figure 2.2:
Victor Hess, discoverer of the cosmic rays after his 1912 balloon flight that reached an altitude of 47,500 feet. (Source: **Friedlander, M. W.** *Cosmic Rays*, 1989)

Cosmic rays have interested scientists for many different reasons. They come from every direction in space, and the origination of many of these cosmic rays is unclear. The discovery of cosmic rays was historically recorded in 1912 by Austrian physicist, Victor Hess¹, who subsequently received the Nobel Prize in Physics for that work. Cosmic rays were originally discovered, because of the ionization they produce in the Earth's atmosphere. An extreme range of incident cosmic ray particles have been used to study in the field of Astrophysics and Particle Physics, which may not be studied in any other way.

In the past, cosmic rays are usually referred as **galactic cosmic rays**, because they come from somewhere that we did not know where they originated. Later scientists found that the Sun emits a significant amount of energetic particles, which plays an important role to the Space Weather phenomena (see section 2.4: Space Weather). Nowadays, we classify cosmic rays into 4 types depending on their sources; that are

- Galactic Cosmic Rays (GCR)

¹Victor Franz Hess, Austrian physicist, born in 1883 and die in 1964. He received the Nobel Prize in Physics in 1936 for the discovery of cosmic ray radiations.

- Cosmic Rays from outside our Galaxy
- Solar Energetic Particles (SEP)
- Anomalous Cosmic Rays (ACR)

The first type is galactic cosmic ray (GCR) with energy ~ 100 MeV to 10^{19} eV, coming from outside our solar system. These particles are predominantly accelerated in our galaxy, the Milky Way. There are many kinds of evidence indicating their sources, e.g., supernova explosion, pulsars, and stellar coronal mass ejections.

The second type, at energy above 10^{20} eV, higher than GCR's range, originated from powerful astrophysical accelerators located outside of the Milky Way. We do not exactly know the source or how can the particles be accelerated to that very high energy.

The third type, mostly protons at energy ~ 100 keV to 50 GeV, are called solar energetic particle (SEP), or in another name-solar cosmic rays. They are accelerated near the surface of the Sun and at coronal mass ejection shocks. Most solar cosmic ray events correlate relatively well with solar flares.² SEP are mostly observed at the peak of the 11-year solar activity cycle when the Sun has maximum activity on its surface.

The fourth type is anomalous cosmic rays (ACR). They are formulated from neutral atoms in the interstellar medium and are ionized by solar ultraviolet radiations or charge exchange with the solar wind.

All of these 4 types can be mentioned as **primary cosmic rays**. When primary cosmic rays enter into the Earth's atmosphere, they can not get far through the air. They collide with nitrogen or oxygen molecules in troposphere³. The collision changes the incident cosmic ray particles and air molecules to several new particles. Any particles created in the atmosphere from collisions are termed

²Solar flare: see section 2.4.1: Solar Activities.

³Troposphere is an inner atmosphere at about 15-30 km above the Earth.

secondary. Kinetic energies from the primary cosmic rays are transferred to each new particle. Secondary cosmic rays spread out and continue to hit another air molecule, generating a cascade of particles showering toward the ground. This process disintegrates into smaller energy of pions, muons and others, and is called **cosmic ray shower.**

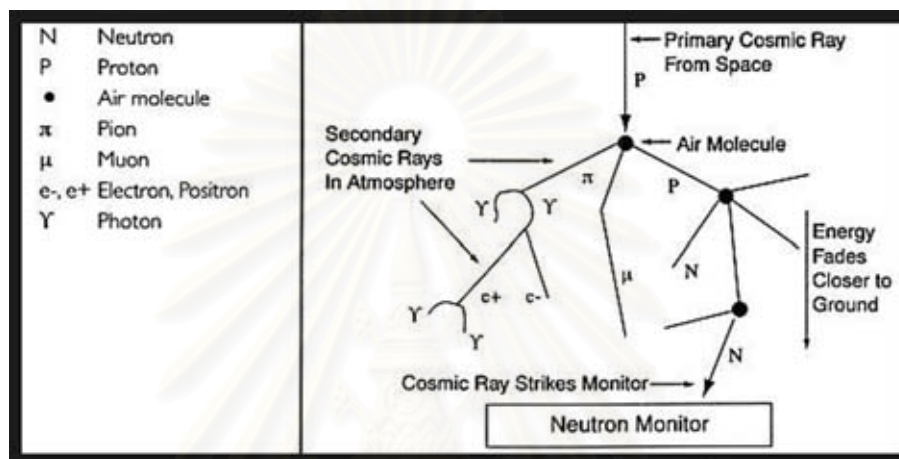


Figure 2.3: Cosmic ray shower diagram. (Source: Bartol Research Institute Neutron Monitor Program: <http://www.bartol.udel.edu/~neutronm/listen/fig2.jpg>)

Figure 2.3 shows a cosmic ray shower diagram. A primary cosmic proton strikes air molecule, creates an array of new particle type that carries portion of energies. A number of secondary cosmic rays in the atmosphere increases to maximum, and then diminishes as the energy fades closer to the ground. High-energy secondary particles are rare, and in contrast, low energy particles are plentiful because of the atmospheric absorption. Neutrons, which are one of product generation created by cosmic ray showers, may be detected on the ground by a neutron monitor.

2.2 Earth's Magnetosphere and Cutoff Rigidity

The Earth's outer-core contains a mixture of liquid metal that always flows around the solid inner-core. The dynamic flowing of the metal is the main mechanism generating Earth's magnetic dipole field. The magnetic field spreads

out from the south geomagnetic pole into outer space and folds up at the north geomagnetic pole, as shown in the Figure 2.4.

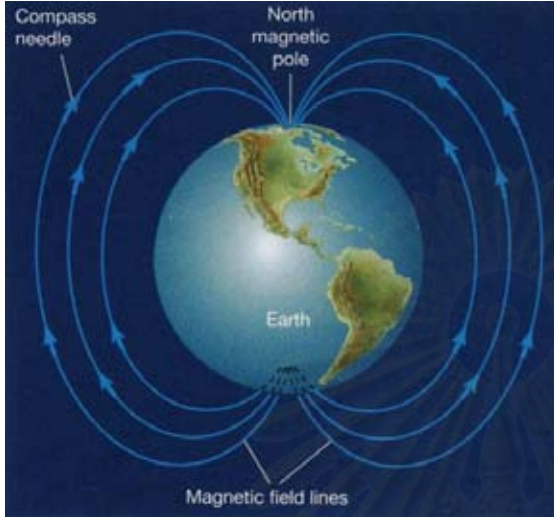


Figure 2.4:
The Earth's magnetosphere. (Source: **Army, Thomas T.**, *Explorations Stars, Galaxies, and Planets*, 2003.)

The Earth's magnetic field may extend in the space farther than 40,000 km. On the ground, the maximum intensity is about 0.5 Gauss. The influence of the Earth's magnetic field directly affects the incoming charged particles, according to the law of the Lorentz force that may change the charged particle's direction when it moves in the magnetic field. For that reason, before the primary cosmic rays reach the atmosphere they need to penetrate the geomagnetic region. The aspect of particle's motion in the magnetic field depends on two parameters; its incoming direction, and its rigidity defined as

$$R \propto \frac{pc}{q}, \quad (2.1)$$

where

p : particle's momentum (GeV/c),

c : speed of light,

q : particle's charges.

Hence, rigidity will have the unit of GV (gigavolts). Since the magnetosphere imposes a lower limit on the energy of primary cosmic ray particles to

enter the atmosphere, the shielding effect of the Earth's magnetic field is usually described by the concept of cutoff rigidities. The reason is that any kind of charged particle with the same rigidity will have the same radius of curvature when it moves in the magnetic field. The radius of curvature, r , is defined as

$$r = \frac{\text{Rigidity}}{B}, \quad (2.2)$$

where B is magnetic field intensity.

Low-energy (or low rigidity) cosmic ray particles which are reaching the Earth's magnetosphere are forced to curve their direction of travel and guided along magnetic field lines. Some of them are guided to fall at geomagnetic poles; however most will be trapped in the region of the Earth's magnetosphere; called **Van Allen Belt**. A simulated cosmic ray orbit, representing the effect of the Earth's magnetic field on incoming charged particles, is shown in Figure 2.5



Figure 2.5: A simulated cosmic ray orbit, representing the effect of the Earth's magnetic field on incoming charged particles. The chaos of each orbit depends sensitively on the particle's rigidity and direction of travel. Some particles spiral around the Earth many times before descending to a low altitude. (Source: **Friedlander, M. W.** *Cosmic Rays*, 1989)

At a specific location, primary cosmic ray particles require sufficient energy to propagate through the Earth's magnetosphere. Only particles having their rigidities greater than the lower limit; called **cutoff rigidity**, will be capable to hit the atmosphere in order to produce secondary particles. Geophysicists use vertical cutoff rigidity instead of geographical latitude when they mention about

incoming cosmic rays. The vertical cutoff rigidity at almost every position on Earth is surveyed and mapped as shown in Figure 2.6.

Figure 2.6 represents the vertical cutoff rigidity map. As we can see in the map, the iso-cutoff line looks strange, not be the same as latitude lines as we might think. This is because, in reality, our Earth does not have a perfect dipole magnetic field. There are some differences from the ideal because of the fluid dynamic in the outer core, which changes the aspect of the map every year.

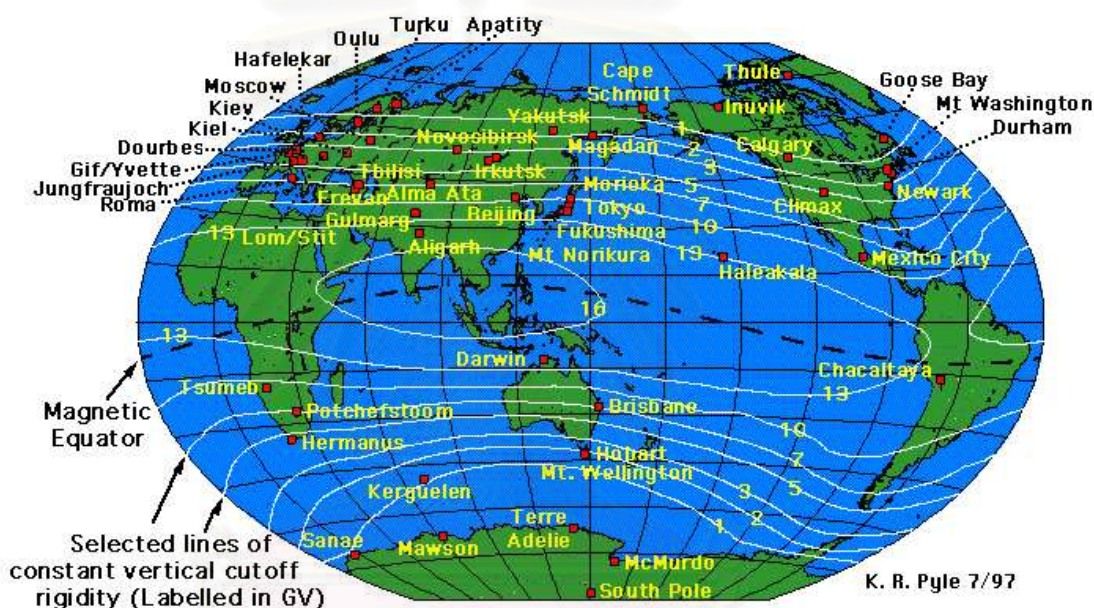


Figure 2.6: Cosmic ray neutron monitors around the world in 1997 and vertical cutoff rigidity map. (Source: Space Physics Data System, Climax and Haleakala Neutron Monitor Datasets: <http://ulysses.sr.unh.edu/NeutronMonitor>)

In the map, we find that Thailand locates in the region which has the highest geomagnetic cutoff in the world (about 17 GV). There is a multinational project organized by Chulalongkorn University (Thailand), Shinshu University (Japan), and University of Delaware (the United States of America), to set a neutron monitor station at Doi Intanon in Chiang Mai Province, northern of Thailand. Monitoring neutrons at Doi Intanon will select only galactic cosmic rays.

Upon completion, the Doi Intanon monitor will be given the name as

the **Princess Sirindhorn Neutron Monitor**, according to the name of a Thai Royal Princess. This station will be the second most sensitive detector of solar neutrons and will be in the top-five worldwide in terms of total galactic cosmic ray count rate. The plan will install 18-tubes NM64 (see Chapter 4: The Neutron Monitor) at latitude of $18^{\circ}35'11''$ North, longitude of $98^{\circ}29'17''$ East, and at altitude 2,565 meters.

The altitude is also significant to detect neutrons because of the atmospheric absorption. The higher above sea level, the more neutrons will be detected. The vital importance of atmospheric absorption will be discussed in the next section.

2.3 Cosmic Rays in the Atmosphere

The sky is not nearly as benign as some might think, even with respect to the cosmic ray shower in the atmosphere. Therefore, from previous sections, atmospheric environment is the result from high-energy cosmic rays (mostly protons) traveling through the Earth's magnetosphere, striking air molecules, and generating a cascade of several particles showering toward the ground.

From Figure 2.3, during a collision, protons, neutrons and other secondary particles are released. Pions, produced in the first generation, may quickly decay in two ways. Neutral pions decay into photons, and charged pions decay into muons. Muons decay into an electron and positron, and a neutrino. Nevertheless, relativistic muons may be observed on the ground because of the time dilation phenomena, when muons travel with a speed close to the speed of light. Sufficient photons from pions decay product can transform into electrons and positrons. Most protons, electrons, positrons, and heavy ions (from multiple collisions with air molecules) are absorbed in the atmosphere by ionization energy loss process.

2.3.1 Neutrons

Neutrons are attenuated by multiple elastic scattering they collide with air molecules. The atmospheric neutrons extend in energy to greater than 1 GeV as can be seen in Figure 2.7 which shows the differential neutron energy spectrum as measured by Hewitt et al (1978).

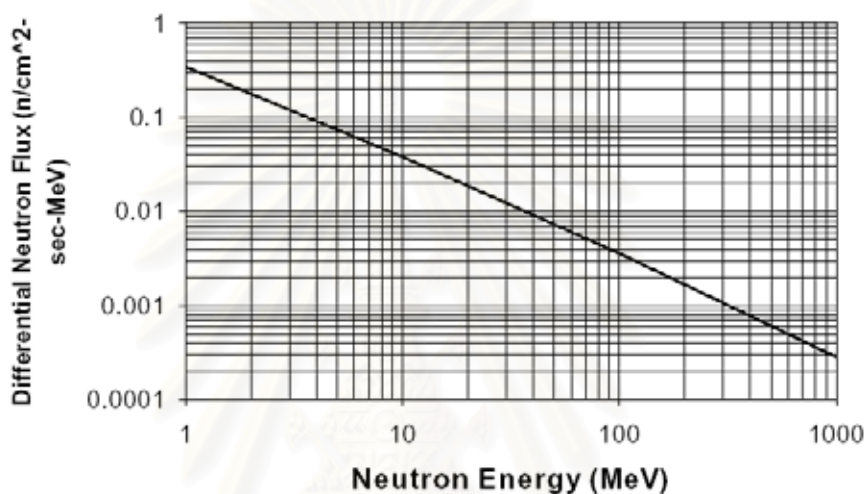


Figure 2.7: Spectrum of the average differential neutron flux in the atmosphere at 40,000 ft. and 45° latitude based on the measurements of NASA-Ames and normalized to a 1-10 MeV neutron flux of 0.85 n/cm² sec [Hewitt et al (1978), Normand (1996), Taber and Normand (1993,1995)].

The amounts of neutron in the atmosphere vary with both altitude and latitude. The altitude variation is shown in Figure 2.8. This curve is a plot of 1-10 MeV atmospheric neutron flux as a function of altitude based on aircraft and balloon measurements [Taber and Normand (1993)]. The maximum neutron flux was measured at about 60,000 feet (~18 km), which is called **Pfotzer maximum**. This result can be representative of the variation of the entire neutron spectrum even it is only for the 1-10 MeV neutrons. Normand and Baker have verified this by observing the same behavior of the 1-100 MeV fluxes as a function of altitude in 1993 [Normand and Baker (1993)].

From Figure 2.8, the curve indicates that at aircraft altitude⁴ of about

⁴ Aircraft altitudes (default altitudes established by the ICAO: International Civil Aero-

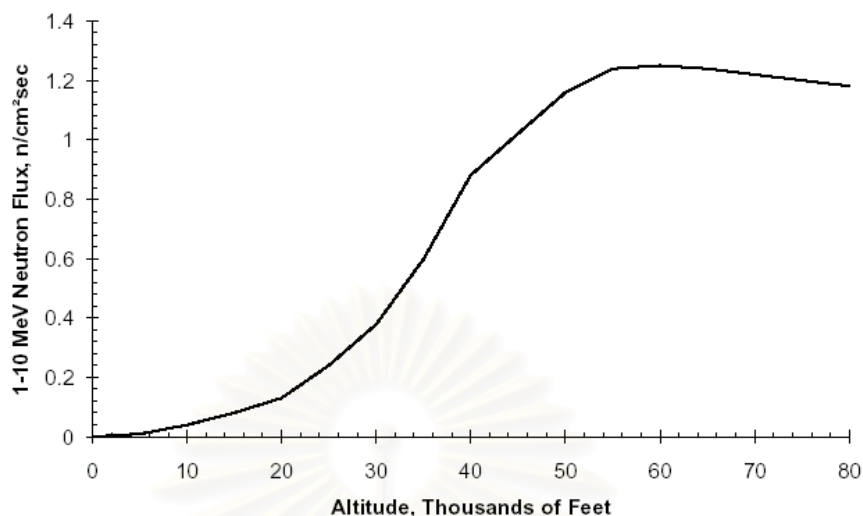


Figure 2.8: The 1-10 MeV atmospheric neutron flux as a function of altitude based on aircraft and balloon measurements [Normand (1996), Taber and Normand (1993)]. Neutrons created by cosmic ray showers peak at about 60,000 ft. At 30,000 ft. the neutrons are about 1/3 of the peak flux, and on the ground, about 1/400 of the peak flux.

30,000 feet, the neutrons are about 1/3 peak flux. Such a significant amount of neutron flux may cause any single event upset (SEU) in aircraft electronics [Normand (1996), Taber and Normand (1993)]. The occurrence of single event effects in avionics is the effects from secondary cosmic ray particles, such as, protons, electrons, pions, but neutrons are the most important.

The latitude variation of the atmospheric neutron flux is shown in Figure 2.9. This result is a plot of 1-10 MeV neutron flux as a function of geographical latitude based on measurements made aboard aircraft at 35,000 feet (~ 10.5 km) [Normand (1996)]. Note that the original data were displayed as a function of vertical rigidity cutoff, and then transformed into the form as a function of geographical latitude. The result implies that at the strongest geomagnetic field the secondary neutrons are rare compared with the location where the geomagnetic field is weakest.

nautical Organization): commercial flight, 28,000-43,000 ft.; concorde and supersonic airplane, 55,000 ft.; high speed civil transport, 55,000-65,000 ft.; jet fighter, 35,000-42,000 ft.; helicopter, 5,000 ft.

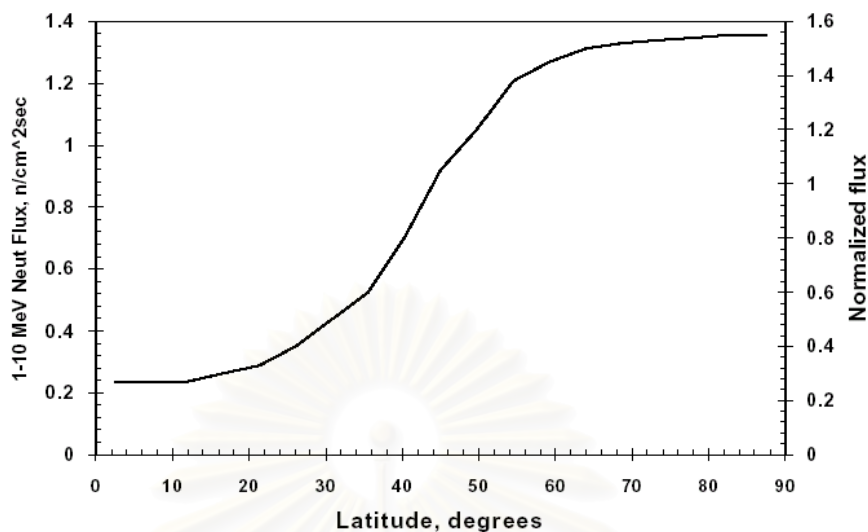


Figure 2.9: The 1-10 MeV neutron flux as a function of geographical latitude based on aircraft neutron measurements [Allkofer and Grieder (1984), Merker et al. (1973), Normand (1993)].

The study of atmospheric absorption is once again important, because there are postulates that link it to the cloud and climate changing. Therefore, neutron counting rate is suspected to be related to ion production in the cloud, and the radiative effect may somehow connect to cloud condensation and temperature variation in the troposphere.

2.4 Space Weather

Space Weather is a term which has become accepted for the past few years to refer to a collection of physical processes, beginning at the Sun's surface and ultimately affecting human activities on Earth and in space. In the past three decades, technologies on Earth have been developed and grown up rapidly, and the public utility system has become much more complicated. Since we depend on these facilities in everyday life, the study of Space Weather is then becoming important to prevent damages from the variation on the Sun's surface.

2.4.1 Solar Activities

The Sun is the main energy source in our solar system. We obtain benefits from the Sun in the form of heat energy and light energy that are coming from nuclear interactions in the core region. The energy emitted by the Sun measured in luminosity on Earth is about $1,450 \text{ W/m}^2$ on average.

In addition to nuclear synthesis drives in the core, there are activities on the surface releasing a energetic flux of particles. These high-energy particles have a variety effects on Space Weather, when they travel close to the Earth. Number of activities on the Sun's surface varies in every 11 years; called solar cycle. The duration when the Sun has the most activity is called **solar maximum**, and **solar minimum** is when the Sun has the least activity. Major events occurring during solar cycle are as follows.

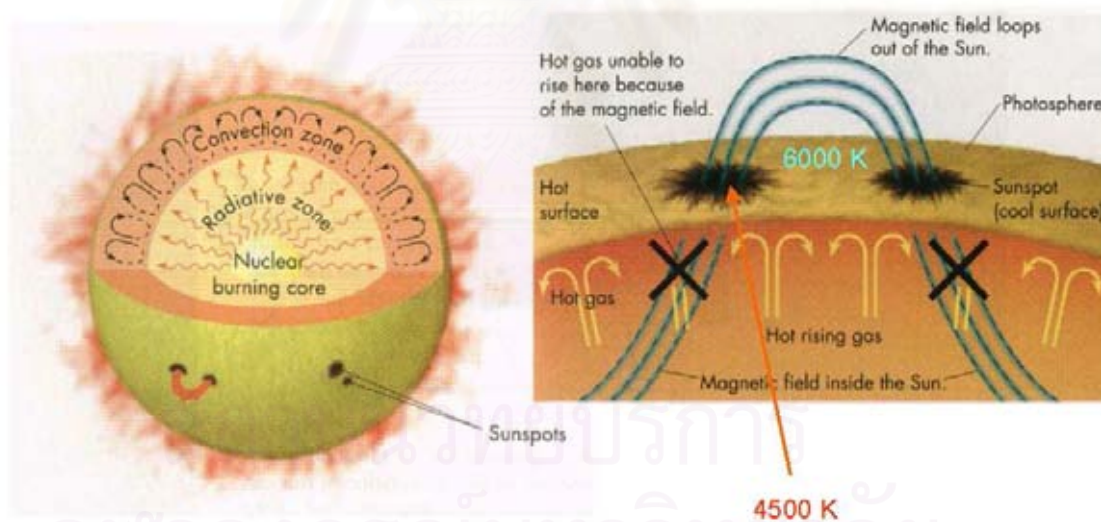


Figure 2.10: The general Sun's structure (left), and sunspots on the surface (right). (Source: Arny, Thomas T., *Explorations: Stars, Galaxies, and Planets*, 2003, page 155,165.)

Sunspots

are a hole on the Sun's surface where magnetic field inside the Sun loops out in the photosphere⁵ and loops into another hole. Sunspot occurs in pairs. At sunspot area the temperature is cooler at about 4,500 K whereas another area is about 6000 K⁶. The reason is that hot gas from convection zone is unable to rise here because of the magnetic field (see Figure 2.10).

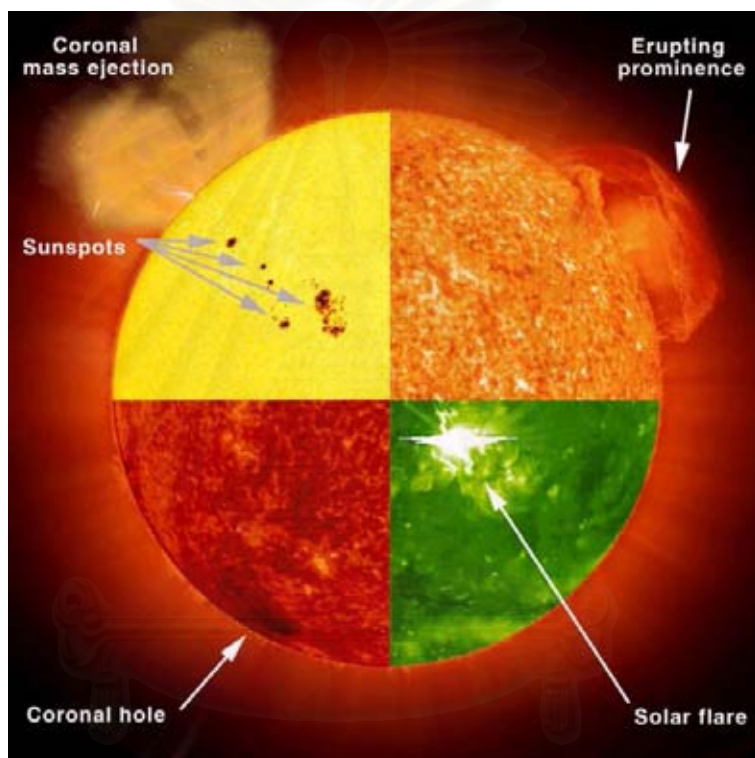


Figure 2.11: Solar Activities. (Source: <http://www.istp.gsfc.nasa.gov>)

Solar Flares

are powerful explosive phenomena occurring at the Sun's surface during solar maximum. Solar flares and related phenomena are shown in Figure 2.11. Flares happen when energy stored in twisted magnetic fields (usually above sunspots) is suddenly released. They are very fast processes lasting only a few minutes.

⁵The Sun's atmosphere can be divided into 3 layer, photosphere, chromosphere, and corona according from the inner layer to outer layer.

⁶from blackbody spectrum

The explosions heat the material on the Sun's surface up to millions of degrees (equivalent to power up to 100 Megaton TNT⁷) and release energy in many forms, i.e., electromagnetic waves (gamma rays and X-rays), mass flows and energetic particles.

Coronal Mass Ejections (CMEs)

are huge gas bubbles ejected from the solar corona⁸ into the interplanetary medium. The ejections, first observed from space in the early 1970s, appear as large magnetic loops whose footpoints are rooted to the solar surface (Figure 2.12). They mostly happen during solar maximum, and large events are associated with so-called **gradual flares**. Up to 10^{13} kg of gas is ejected outward at speeds ranging from 100-2,500 km/s. CMEs can move at supersonic speeds, i.e., exceeding the local sound speed. At such a supersonic speed, they cause magnetic field distortion and form shock waves in front of them, which are known as interplanetary shocks. When CMEs travel closely to Earth, they cause important effects on Space Weather.

2.4.2 Effects on Everyday Life of Humans

Space Weather phenomena have a variety of effects to us. Energetic particles can directly damage on equipments both in space and on the ground. Moreover, the explosions on the Sun's surface producing radiations and abundance of particles, cause interaction with the Earth's magnetic field and outer atmosphere in complex ways. These can result in geomagnetic variation affecting a number of technologies.

⁷TNT: Trinitrotoluene, an explosive

⁸Corona is an outer layer of the Sun's atmosphere which extends beyond inner layers into interplanetary space. This layer covers a large volume all around the Sun having a temperature of about 10^6 K.

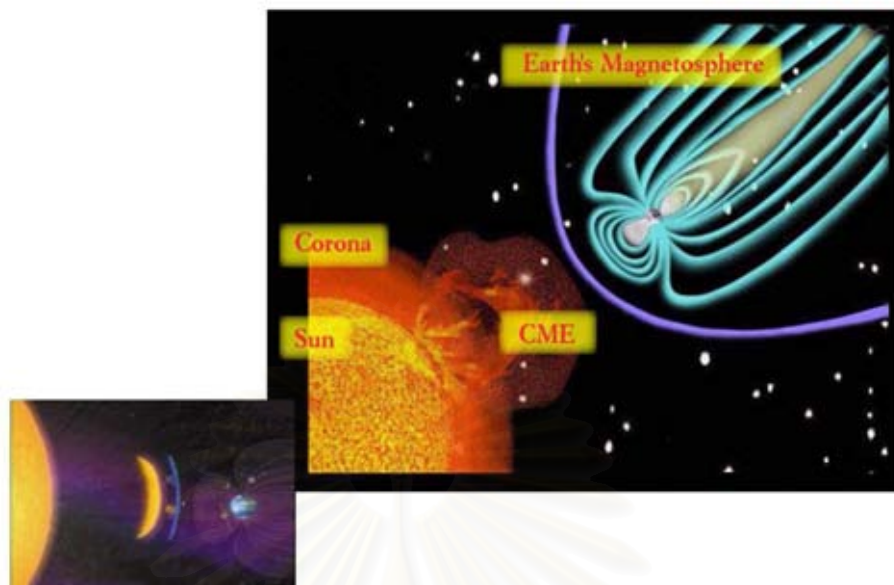


Figure 2.12: The coronal mass ejection. The Sun emits a huge bubble from the solar corona into the interplanetary medium (right), and (left) the ejection expands its size during propagating toward the Earth with a supersonic speed which following forms shock waves in front of it.

Geomagnetic Variation

During magnetic storm events on the Sun's surface, the magnetic field and energetic particles which are thrown out, interact with the Earth's magnetosphere produce geomagnetic disturbances and increase ionization in the ionosphere.⁹ The increased ionization affects communication or GPS¹⁰ navigation using radio waves. The geomagnetic disturbances have various effects on Earth. They directly affect operations using geomagnetic field, such as directional drilling, magnetic surveys, or compass used in navigation. Furthermore, geomagnetic disturbances also induce electric currents (called **geomagnetically induced current: GICs**) in long conductors, such as power lines and pipelines, causing power system outages or pipeline corrosion.

⁹Ionosphere is an outer atmosphere at 100 to 1,000 km above the Earth. At this layer the neutral gas atoms (or molecules) are ionized into free electrons and positive ions by intensively incoming solar radiations. The ionized electrons can exist for a short period of times before they are captured by nearby positive ions. This region has properties of plasma that can reflect some acceptable wave range of electromagnetic waves.

¹⁰GPS: Global Position System

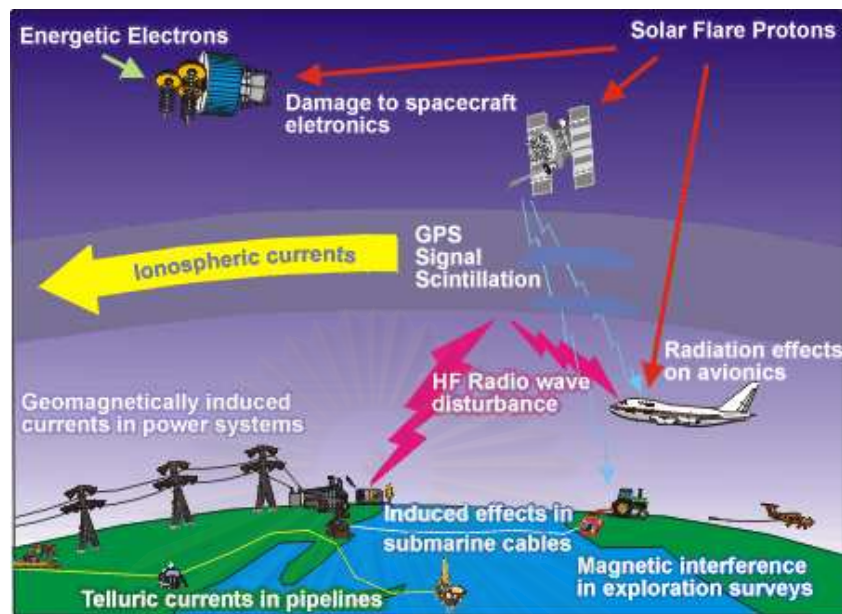


Figure 2.13: A variety of effects from Space Weather phenomena. Solar energetic particles can damage to electronics in spacecraft and satellites. Primary cosmic rays can cause radiation effects on avionics, and secondary particles may cause single event upset in aircraft electronics. The increased ionization in ionosphere may disrupt radio communication. Geomagnetic disturbances affect navigation system that use geomagnetic field, and cause power system outages and pipeline corrosion. (Source: Space Weather Canada: <http://www.spaceweather.gc.ca>)

Power Systems

The geomagnetic disturbances and accumulative charged by solar cosmic rays may cause current flow in ionosphere; called **ionospheric current** or **auroral current**. This current is up to millions of Ampère and induces potential magnetic field according to the Ampère's law. The induced magnetic field is dense at geomagnetic poles and varies in times because of geomagnetic disturbances. The times variation of this induced magnetic field produces temporary DC currents (GICs) in long conductor such as power lines and pipelines.

Geomagnetically induced currents are up to 100 Ampère that can have serious effects on power systems. GICs in power lines flow to ground through substation transformers and then saturate the core of the transformers that finally lead to many different problems. Increased heat has caused the transformers to burn out. Extra harmonics generated in the transformers produce unwanted relay

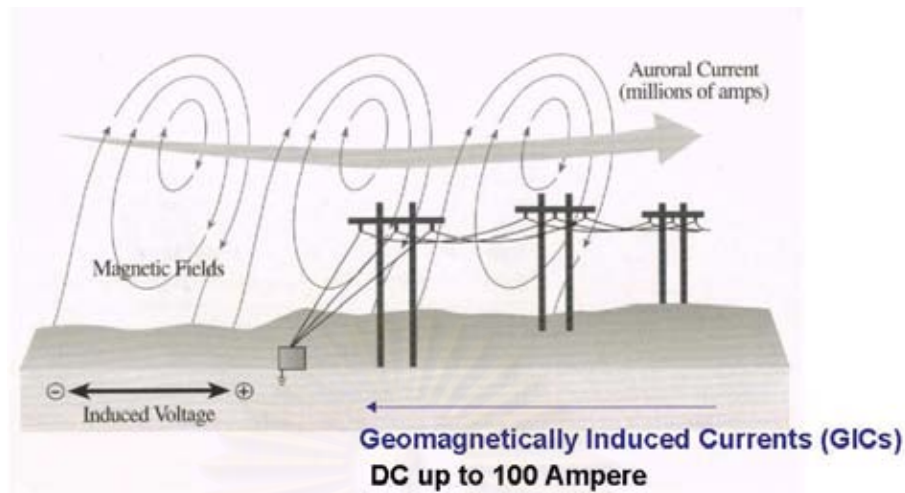


Figure 2.14: Effects on power systems. Currents in the ionosphere induce magnetic field which subsequently induces currents along power lines; called geomagnetically induced currents (GICs). GICs occur in DC current which may be up to 100 Ampère and destroy transformer. The effect of GICs can cause serious problems on power systems that may ultimately lead to power system outages and electrical blackout. (Source: **Lang, Kenneth, R.**, *The Cambridge Encyclopedia of the Sun*, 1st ed., 2001, page 174.)

operations. These can affect to the stability of the power systems and lead to out of service. Such a sequence has been occurred in Quebec (Canada) with an electrical blackout in the winter of 1989 which left the whole province without power for over 9 hours. The damages from this event cost more than \$13.2 millions.

Pipelines

Pipelines are used to transfer water, oil, or gas in long distances that are mostly placed underground. Pipelines can be affected by GICs since they are made from metal. The current flows in pipelines lead to chemical reaction between the material and humidity causing metal corrosion.

In case of communication cables, GICs produce some noise currents that annoy communications.

Satellites and Space Shuttles

Radiations from the Sun may lead to the expansion of the atmosphere. Here, it causes friction force to the satellites orbiting above the Earth. The satellites affected from friction force will alter their orbits into unstable points, ultimately fall down to the ground.

Another problem is from the energetic particles impacting on solar cells and semi-conductor devices on the satellites and space shuttles. This can cause anomaly function in the decision circuits and make some devices out of use.

Global Position Systems and Radio Communications

At the ionosphere, the solar radiations (UV and X-rays) ionize air molecules into free electrons and positive ions. Therefore, ionosphere has a property of plasma being enable to reflect and transparent radio waves. The performance of plasma to reflect or transparent radio waves depends on the plasma frequency, f_p , defined as

$$f_p = \sqrt{81N_e} \text{ Hz}, \quad (2.3)$$

where N_e is number of free electrons per cubic meter. Radio wave can reflect the medium only if their frequencies are lower than plasma frequency, otherwise they can transparent through the plasma. Since f_p directly depends on number of free electrons that ionized from solar radiations, and solar radiations are abundant depending on solar activity. Then we can imply that the reflecting of the radio waves at the ionosphere is related to the solar activities. The solar activities may affect the radio communications by disruption radio transmission from satellites to the ground base stations. The increased ionization can cause communication signal delay and wrong GPS positioning.

Health Risks

Solar radiations can be hazardous to astronauts in the space. In addition, the radiation can damage to the electronics devices on aircraft causing risks during journey. The magnetic disturbances can disrupt communication between jet planes and control base stations leading to navigation system failures.



สถาบันวิทยบริการ
จุฬาลงกรณ์มหาวิทยาลัย

Chapter 3

Neutron Physics and Neutron Detection

As the uncharged member of the nuclear pair, the neutron plays a fundamental role in the study of nuclear force. Because it is electrically neutral the neutron is unaffected by the Coulomb barrier. Low energy (eV or less) neutron can penetrate the nucleus and initiate nuclear reaction resulting in secondary product. The lack of Coulomb interaction leads some experimental problems when using neutrons as a nuclear probe: energy selection and focusing of an incident neutrons beam are difficult. Furthermore, they do not produce primary ionization events in detectors (neutrons passing through matter have negligible interactions with the atomic electrons).

3.1 The Discovery of the Neutron

The first experimental observation of the neutron occurred in 1930 (11 years after Rutherford discovered the proton in 1919), since it was discovered by Bothe and Becker that beryllium, when bombarded by alpha particles (from radioactive decay), emitted a very energetic stream of nonionizing radiation. This stream is unaffected upon magnetic field, and was thought to be gamma radiation. Soon thereafter, Curies and Joliot noticed that when radiated this stream on hydrogen-rich material like paraffin, a 5.3 MeV proton was emitted. Their calculation indicates that if the suspected radiation was gamma ray, its incidental energy should be at least 52 MeV to release such an energetic proton. An emitted gamma ray of such energy seemed extremely unlikely.

In 1932, James Chadwick repeated and expanded this experiment and then proposed that this particle was Rutherford's neutron. He is generally cred-

ited to be the discoverer of the neutron and subsequently awarded the Nobel Prize in 1935 for his discovery. Using kinematics, $s = vt$, and then through conservation of momentum, Chadwick was able to determine the mass of the neutron. He announced this equation:



Figure 3.1: James Chadwick, English physicist, born in 1891 and died in 1974. He had been working under Rutherford in the Physical Laboratory in Manchester for 2 years. In 1932 he made a fundamental discovery in the domain of nuclear physics: he proved the existence of neutrons by bombarding beryllium with alpha particles. In 1935 he received the Nobel Prize in Physics for the discovery of the neutron.

The Free neutron is unstable against β -decay. The equation is



with a half-life of 10.6 minutes. The bound neutron in nuclei may be much longer-lived (even stable) or much shorter-lived: it may convert into proton depending on the state of the nuclei. A neutron could convert into its antiparticle—the antineutron, and then back again to a neutron, according to the prediction from the so-called *Grand Unified Theories*. No evidence has yet been seen for this effect, but current research is trying to search beyond our present knowledge.

3.2 Neutron Sources

Beam of neutrons can be produced from a variety of nuclear reactions. There are five possible neutron sources, which may come from

- Alpha-bombardment
- Photoneutron Source
- Spontaneous Fission
- Nuclear Reactions
- Reactor Sources

Alpha-bombardment

The reaction use beryllium as the target. The equation is



The Q-value for this reaction is 5.7 MeV. This reaction is responsible for the discovery of the neutron, and can be used to produce a suitable beam of neutron in the laboratory.

Photoneutron Sources

We can use (γ, n) reaction to produce neutrons, for example:

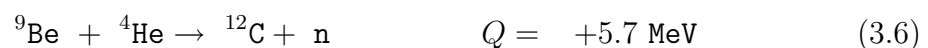


Spontaneous Fission

A common source of neutrons is the spontaneous fission of isotopes such as ${}^{252}\text{Cf}$ (2.65y). From the fission process, neutrons are emitted at a rate of about 4 per fission.

Nuclear Reactions

There are many nuclear reactions that produce neutrons. Some reactions that might be involved are





Reactor Sources

The energy spectrum near the core of the reactor extends to 5-7 MeV, but peak at 1-2 MeV. These neutrons will be moderated to thermal energy using D_2O as the shield. There are also fast neutrons present in the core of the neutron. The high neutron fluxes from a reactor are useful in variety analyses.

3.3 Neutron Attenuation

Neutrons are attenuated by three major interactions; nuclear collision, elastic scattering, and absorption. At high energy (20 MeV or higher), nuclear collision with high atomic nuclei is the major concern. In this case, another new product (neutrons and another kind of particles) is produced through the inelastic collision. At the range of eV to a few MeV, the elastic scattering contributes a large cross-section. This process transfers energy to the recoiling (charged) nuclei, resulting in slowing neutron, and is call **moderation**.

Scattering slows the neutron down as energy is lost in successive collision. The neutron may be slow down, if the absorption cross-section is relatively small, until it comes into thermal equilibrium with its surroundings. Such neutron is called thermal neutron, with kinetic energy 0.025 eV, and can be easily detected because it is captured-which finally release some detectably charged particle radiations. Indeed, it is particularly easy to detect because neutron absorption cross-sections for many material are peak at low neutron energy.

Neutron Moderation

Consider a non-relativistic, elastic collision between a neutron (mass m), with energy E_0 and speed v_0 , incident on a target nucleus (mass M) initially at rest.

This event is illustrated in Figure 3.2, (a) for laboratory (lab) frame and, (b) for center-of-mass (cm) frame.

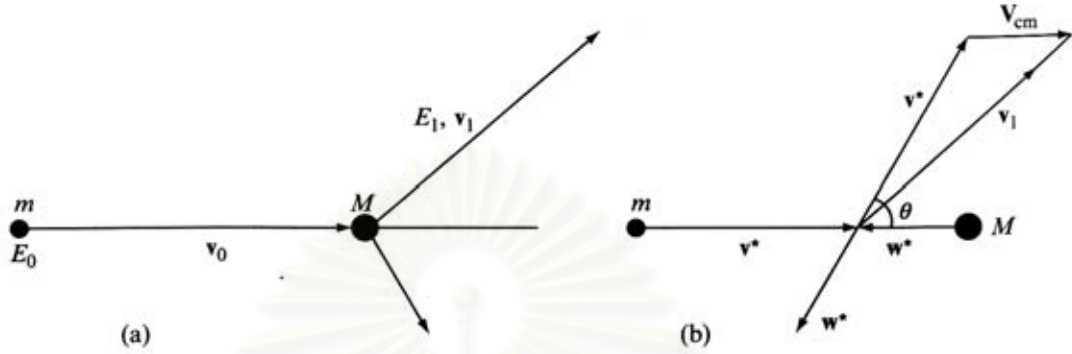


Figure 3.2: Elastic scattering kinematics for an incident particle of mass m , initial energy, E_0 and speed v_0 , colliding with a particle of mass M in (a) the laboratory and (b) the center-of-mass frames of reference.

In the lab frame, the scattered neutron has energy E_1 and speed v_1 . The speed of the center-of-mass, V_{cm} is defined by

$$mv_0 = (m + M)V_{cm} \quad (3.9)$$

$$V_{cm} = \frac{mv_0}{m + M} \quad (3.10)$$

The incident speed of the neutron between lab and cm frames is related by

$$v_0 = v^* + V_{cm} \quad (3.11)$$

Substituting this v_0 into Eq.(3.9) yields

$$v^* = \frac{v_0 M}{m + M} \quad (3.12)$$

In the center-of-mass frame, Figure 3.2(b), the vector summation

$$\vec{v}_1 = \vec{v}^* + \vec{V}_{cm} \quad (3.13)$$

Squaring (dot product) this equation gives

$$v_1^2 = v^{*2} + V_{cm}^2 + 2v^*V_{cm} \cos \theta \quad (3.14)$$

Using v^* from Eq.(3.12) and V_{cm} from Eq.(3.10) hence

$$\frac{v_1^2}{v_0^2} = \frac{M^2 + m^2 + 2mM \cos \theta}{(m + M)^2} \quad (3.15)$$

From the conservation of energy, E

$$\frac{E_1}{E_0} = \frac{v_1^2}{v_0^2} \quad (3.16)$$

Apply this kinematics in to Eq.(3.15) yields

$$E_1 = E_0 \left[\frac{M^2 + m^2 + 2mM \cos \theta}{(m + M)^2} \right] \quad (3.17)$$

Notes that θ is the scattering angle in the center-of-mass frame, but E_1 and E_0 are measured in the laboratory frame. The scattering angle, θ , varies from 0° to 180° . If $\theta = 180^\circ$, and substitute neutron mass with 1 and target mass with A , this gives

$$\begin{aligned} E_1(\min) &= E_0 \left(\frac{A-1}{A+1} \right)^2 \\ &= \alpha E_0 \end{aligned} \quad (3.18)$$

where $\alpha \equiv \left[\frac{A-1}{A+1} \right]^2$. Notice that for $A = 1$ (scattering from hydrogen nucleus), the neutron transfers all its energy to the stuck proton.

Next, to determine the effect of the scattering on the average neutron energy, we calculate the probability distribution $P(E_1)dE_1$ of the scattered neutron having the energy between E_1 and E_1+dE_1 . From Eq.(3.17) there is a one-to-one correlation between E_1 and scattering angle in cm frame, θ . Hence the probability distribution in angle is

$$-p(\theta)d\theta = P(E_1)dE_1 \quad (3.19)$$

The negative sign on the left-hand side of Eq.(3.19) allows for the fact that the energy decreases as the angle increases.

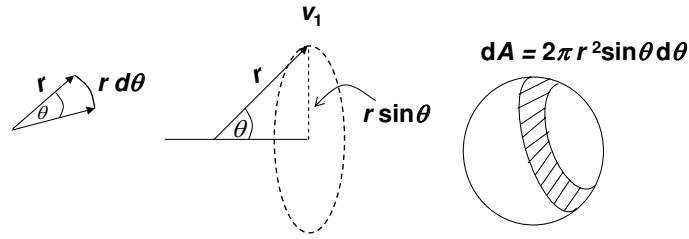


Figure 3.3: Considering the probability of the scattering neutron (in cm frame) between the scattering angle θ and $\theta + d\theta$. Note that \vec{r} is a radius vector rotating from $\theta = 0^\circ$ to $\theta = 180^\circ$, and from $\phi = 0^\circ$ to $\phi = 360^\circ$.

For s-waves, elastic scattering is isotropic in the cm frame. If v_1 has a constant size of r , from Figure 3.3, $p(\theta)$ is denoted by small area on the sphere between θ and $\theta + d\theta$, $A_{\theta \rightarrow \theta + d\theta}$, divided by total area on the sphere. Since

$$\begin{aligned} dA &= 2\pi(r \sin \theta)d(r\theta) \\ &= 2\pi r^2 \sin \theta d\theta \end{aligned} \quad (3.20)$$

and total area on the sphere, A_{total}

$$A_{total} = 4\pi r^2 \quad (3.21)$$

Hence, the angular distribution probability

$$\begin{aligned} p(\theta)d\theta &= \frac{dA}{A_{total}} \\ &= \frac{2\pi r^2 \sin \theta d\theta}{4\pi r^2} \\ &= \frac{1}{2} \sin \theta d\theta \end{aligned} \quad (3.22)$$

Note that large angular momenta become increasingly important at higher neutron energies.

Back to Eq.(3.17), assign the neutron mass, $m = 1$, and the target mass, $M = A$, this gives

$$E_1 = E_0 \left[\frac{A^2 + 1 + 2A \cos \theta}{(A + 1)^2} \right] \quad (3.23)$$

The derivative of the scattered energy by θ is

$$\begin{aligned}\frac{dE_1}{d\theta} &= -\frac{2AE_0 \sin \theta}{(A+1)^2} \\ &= -\frac{2AE_0 \sin \theta}{(A+1)^2} \left[\frac{-P(E_1)dE_1}{p(\theta)d\theta} \right]\end{aligned}\quad (3.24)$$

Note that, according from Eq.(3.19), $\frac{-P(E_1)dE_1}{p(\theta)d\theta} = 1$. Then substitute $p(\theta)d\theta$ with $\frac{1}{2} \sin \theta d\theta$ from Eq.(3.22), hence

$$\frac{dE_1}{d\theta} = -\frac{2AE_0 \sin \theta}{(A+1)^2} \left[\frac{-P(E_1)dE_1}{\frac{1}{2} \sin \theta d\theta} \right] \quad (3.25)$$

And do some arithmetics, we find

$$\begin{aligned}P(E_1)dE_1 &= \frac{(A+1)^2 dE_1}{4AE_0} \\ &= \left(\frac{1}{1-\alpha} \right) \frac{dE_1}{E_0} \\ P(E_1) &= \left(\frac{1}{1-\alpha} \right) \frac{1}{E_0}\end{aligned}\quad (3.26)$$

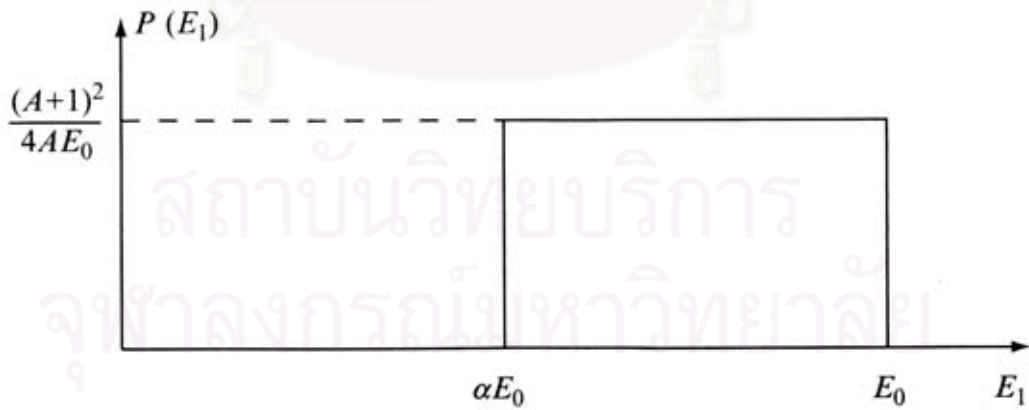


Figure 3.4: Probability distribution for neutrons (with initial energy E_0) having a final energy E_1 after being elastic scattering by a stationary target with mass number A . It is assumed that the scattering is isotropic in the center-of-mass frame; $\alpha \equiv [(A-1)/(A+1)]^2$.

The distribution in energy after one scattering will be uniform between $E_1(\min) = \alpha E_0$ and E_0 , as illustrated in Figure 3.4. Note that the quantity

$(1 - \alpha)E_0$ is the range of all post-collision energies, the average neutron energy after the collision is $\bar{E}_1 = \frac{1}{2}(1 + \alpha)E_0$, and the average energy loss, \bar{E}_{loss} , is $\frac{1}{2}(1 - \alpha)E_0$. If we try to calculate the n^{th} scattering, we get

$$\begin{aligned}\bar{E}_1 &= \frac{1}{2}(1 + \alpha)E_0 \\ \bar{E}_2 &= \frac{1}{2}(1 + \alpha)E_1 \\ \bar{E}_3 &= \frac{1}{2}(1 + \alpha)E_2 \\ &\vdots \\ \bar{E}_n &= \frac{1}{2}(1 + \alpha)E_{n-1}\end{aligned}$$

After some arithmetic, we find

$$\bar{E}_n = \left[\frac{1}{2}(1 + \alpha) \right]^n E_0 \quad (3.27)$$

and

$$\bar{E}_n = E_0 \left(\frac{\bar{E}_1}{E_0} \right)^n \quad (3.28)$$

These two equations are not the most useful measure of the average neutron. Although each neutron will scatter many times, we must repeat the energy loss calculation. In the case of the second scattering, the incident neutrons are no longer monoenergetic (distributed between αE_0 and E_0).

To make the calculations better characterize the distribution, we introduce the **logarithmic energy decrement** parameter, ξ , to represent the average value of $\ln(E_0/E_1)$ after a first collision:

$$\xi = \overline{\ln(E_0/E_1)} = \int_{\alpha E_0}^{E_0} \ln \frac{E_0}{E_1} P(E_1) dE_1 \quad (3.29)$$

Substituting $P(E_1)$ from Eq.(3.26) into in this equation and hence

$$\xi = \frac{1}{(1 - \alpha)E_0} \int_{\alpha E_0}^{E_0} \ln \frac{E_0}{E_1} dE_1 \quad (3.30)$$

Let $x \equiv \frac{E_1}{E_0}$, $dx = \frac{dE_1}{E_0}$ and then substitute into the previous equation, hence

$$\xi = \frac{1}{(1-\alpha)} \int_{\alpha}^1 \ln \frac{1}{x} dx \quad (3.31)$$

Consider

$$\begin{aligned} d(x \ln x) &= \ln x dx + x d(\ln x) \\ &= \ln x dx + x \left(\frac{1}{x} dx \right) \\ &= \ln x dx + dx \\ \int_1^{\alpha} \ln x dx &= \int_0^{\alpha \ln \alpha} d(x \ln x) - \int_1^{\alpha} dx \\ &= \alpha \ln \alpha - \alpha + 1 \end{aligned} \quad (3.32)$$

Substitute this into Eq.(3.31), we find

$$\begin{aligned} \xi &= \frac{1}{(1-\alpha)} \int_1^{\alpha} \ln x dx \\ &= \frac{1}{(1-\alpha)} \left[\alpha \ln \alpha - \alpha + 1 \right] \\ &= 1 + \frac{\alpha \ln \alpha}{1-\alpha} \end{aligned} \quad (3.33)$$

Resubstitute $\alpha = (A-1)/(A+1)$ into the last equation, then we get

$$\begin{aligned} \xi &= 1 + \frac{(A-1)^2}{2A} \ln \left(\frac{A-1}{A+1} \right) \\ &\approx \frac{2}{A} - \frac{4}{3A^2} \end{aligned} \quad (3.34)$$

This equation is approximated by using power expansion of $1/A$ which is accurate to better than 1% for $A \geq 6$. Table 3.1 lists values of ξ for a number of different material. Next, take a look at the definition of ξ ,

$$\begin{aligned} \xi \equiv \overline{\ln(E_0/E_1)} &= \overline{\ln E_0} - \overline{\ln E_1} \\ &= \overline{\ln E_0} - \overline{\ln E_1} \\ \therefore \overline{\ln E_1} &= \overline{\ln E_0} - \xi \end{aligned} \quad (3.35)$$

Note that E_0 is the stationary value, then $\ln E_0$ can be taken out from the average bar. If the neutron scatter the target n times, Eq.(3.35) should be

$$\begin{aligned}
 n = 1 \quad \overline{\ln E_1} &= \ln E_0 - \xi \\
 n = 2 \quad \overline{\ln E_2} &= \ln E_1 - \xi \\
 n = 3 \quad \overline{\ln E_3} &= \ln E_2 - \xi \\
 &\vdots = \vdots \\
 n = m \quad \overline{\ln E_m} &= \ln E_{m-1} - \xi
 \end{aligned}$$

Doing some arithmetics, we finally get

$$\begin{aligned}
 \overline{\ln E_n} &= \ln E_0 - n\xi \\
 n &= \frac{1}{\xi} \left[\ln E_0 - \overline{\ln E_n} \right] \\
 \therefore n &= \frac{1}{\xi} \ln \frac{E_0}{E'_n} \tag{3.36}
 \end{aligned}$$

where $\overline{\ln E_n} \equiv \ln E'_n$, and E'_n represents the neutron energy after n^{th} collision. This solution is very useful to estimate the number n of collision require to slow the neutrons down from their initial energy E_0 to their median energy after n collisions, E'_n . If the initial energy of the neutrons are typically 2 MeV, the number of times to reduce their energy to thermal environment in some commonly used moderator are displayed in Table 3.1.

Table 3.1: Scattering properties of several nuclei.

Nucleus	α	ξ	n (to thermalize)
^1H	0	1.00	18
^2H	0.111	0.725	25
^4He	0.360	0.425	43
^{12}C	0.716	0.158	115
^{206}Pb	0.981	0.0097	1880
^{238}U	0.983	0.0084	2200

As illustrated in Table 3.1, hydrogen is the most suitable element that can be used to slow down the neutron. Practically, we use hydrogen-rich material such as low density polyethylene (in NM64¹¹) and paraffin (in IGY) as the moderator.

3.4 Slow Neutron Detection

As discussed in the previous section, an energetic neutron is moderated (in energy) by elastic scattering. At this moment we have just known how a neutron interact with the medium, but it still cannot be practically detected. Therefore, a neutron detector does not record the presence of the neutron directly but responds to the secondary ionization trail from charged radiations when the neutron undergoes a nuclear reaction in the detector medium. Possible products when a slow neutron collides with a target nucleus are

- recoil nucleus
- proton
- alpha particle
- fission fragments

The first one is responsible for an elastic scattering which is referred in the previous section. The last one, fission fragments, occur when a slow or thermal neutron hits the heavy target nucleus such as plutonium or uranium. This process is commonly used in producing atomic bomb. For the 2nd and 3rd ones, proton and alpha particle, are from neutron absorptions with particular target nuclei.

This section will concentrate on the absorption process used for the detection of the neutron. Figure 3.5 shows the energy dependence of several neutron reaction.

A. The $^{10}\text{B}(\text{n},\alpha)^7\text{Li}$ Reaction

¹¹see Chapter 4: The Neutron Monitor

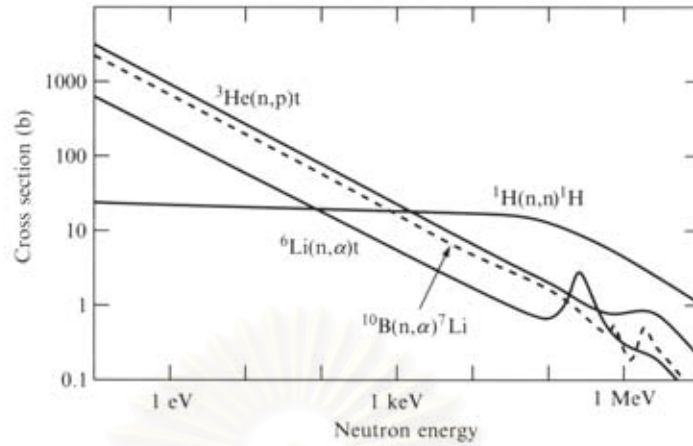


Figure 3.5: Energy dependence of cross sections for neutron absorptions on ^3He , ^6Li and ^{10}B and for total scattering by ^1H . (Source: **Lilley**, *Nuclear Physics-Principles and Applications*, John Wiley & Son, 2001, page 166.)

When thermal (or slow) neutron hits a target nucleus, the reactions are



The cross-section of these reactions follow a $1/v$ dependence, being about 3,820 barns at thermal environment (1/40 eV). The reactions leaves a lithium ion, which is shared between ground state (6%) and excited state (94%), and an outgoing alpha particle. The excited Li falls into ground state and emits a 0.48 MeV gamma ray with a half-life of about 10^{-13} seconds.

Using Q-Value from the excited state (most probability), we can calculate the kinetic energy of the products. From the conservation of the energy,

$$E_{\text{Li}} + E_{\alpha} = Q$$

$$\frac{1}{2}m_{\text{Li}}v_{\text{Li}}^2 + \frac{1}{2}m_{\alpha}v_{\alpha}^2 = 2.31 \text{ MeV} \quad (3.37)$$

And combine with the conservation of momentum,

$$m_{\text{Li}}v_{\text{Li}} = m_{\alpha}v_{\alpha}$$

$$\therefore v_{\alpha} = \frac{m_{\text{Li}}v_{\text{Li}}}{m_{\alpha}}$$

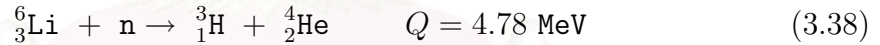
Substitute v_α into Eq.(3.37), and after doing some arithmetics we find that

$$\begin{aligned} E_{Li} &= \frac{Qm_\alpha}{m_\alpha + m_{Li}} = 0.84 \text{ MeV} \\ E_\alpha &= Q - E_{Li} = 1.47 \text{ MeV} \end{aligned}$$

The isotope ^{10}B is generally 19.8% in natural, and commonly used in the form of BF_3 gas inside the proportional counter. The BF_3 is both the target for the nuclear reaction and the counter fill gas. The charged products cause ionization in the detector gas, which gives rise to an output signal. The gamma emission may not leave significance in the gas chamber. The outputs from the proportional counter are displayed in section 5.1 both from experiments and simulation program.

B. The $^6\text{Li}(\text{n},\alpha)^3\text{H}$ Reaction

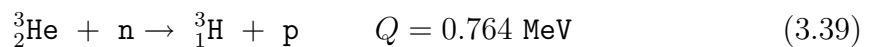
This reaction leaves a fast tritium ion with an energetic alpha radiation. The reaction emits only ground state ions. The equation is



Using the conservation of energy and momentum, as done in the previous reaction, we can get the kinetic energy of the tritium ion, $E_t = 2.73 \text{ MeV}$, and alpha particle, $E_\alpha = 2.05 \text{ MeV}$. The isotope ^6Li is generally 7.40% in natural, but easily purified from substance.

C. The $^3\text{He}(\text{n},\text{p})^3\text{H}$ Reaction

This reaction use isotope ^3He as the target for nuclear reaction and also the counter filled gas. The reaction is



The energy released from this reaction is smaller than for ^{10}B capture, but the signal is still easily detectable and the reaction cross section is almost 40% higher.

Using the conservation of energy and momentum, we can determine for the kinetic energy of the products and find that for a tritium ion, $E_t = 0.573$ MeV, and a proton, $E_p = 0.191$ MeV.

3.5 The Proportional Counter

As discussed earlier, a slow neutron is captured by a target nucleus and then the charged particles are emitted in the gas-filled chamber. This chamber is also functional to be an counter for charged particles. The counter uses an electric field to separate and count the ions (or electrons) by the concept of ionization.

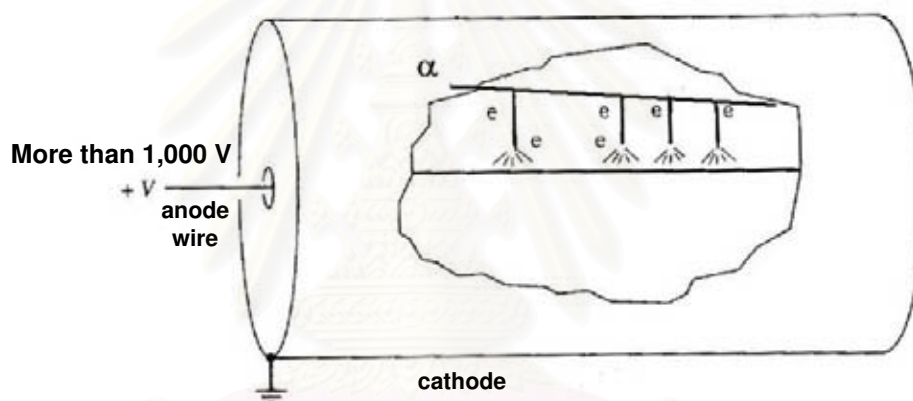


Figure 3.6: The geometry of a filled-gas proportional counter. The incoming (or occurring) radiation creates an ion pair which will be separated by electric field. If we apply high voltage (more than 1,000 volts), the ions will be accelerated rapidly and then collide the medium gas molecules, producing a cascade of many secondary ionizations. The picture has been modified from **Krane, K.S.**, *Introductory Nuclear Physics*. John Wiley & Son, 1988, page 205.

In air, the average energy needed to ionize a neutral gas molecule into an ion and electron pair is about 34 eV; thus a 1-MeV radiation may produce a maximum of about 3×10^4 ion and electron pairs.

The amplitude of the signal is due to the number of ions formed, and thus to the energy deposited by the radiations. For a typical voltage of roughly 100 V, the ions drift slowly to the electrodes compare to a weak radioactive source such as a μCi (which gives an average one decay for every 30 μs). To observe individual pulses in the gas-filled chamber, we must provide a substantial amplification. One

way to perform this is to increase the electrode voltage to higher values, usually in excess of 1,000 V. Such a greater electric field, the ion pair will be accelerated and may acquire enough energy to collide with the medium and create many new ionized ions and electrons (which will be accelerated in turn).

This rapid amplification through production of secondary ionization is called a **Townsend avalanche**. However, there are a large number (perhaps $10^3 - 10^5$) of secondary events for each original ionization. The chamber is particularly operated such that the number of secondary events is proportional to the number of the primary events, and the device is in consequently well defined as a **proportional counter**.



สถาบันวิทยบริการ
จุฬาลงกรณ์มหาวิทยาลัย

Chapter 4

The Neutron Monitor

4.1 Timeline of Early Discovery

During the late 1940s, John Simpson discovered that the latitude variation of the evaporation neutron density in the atmosphere is several times larger than that of the ionizing and hard component [Simpson (1948)].

The following year, he found that the latitude dependence of the nucleonic component was equal to that of atmospheric evaporation neutrons at 30,000 ft. [Simpson (1949a)].

The discovery inspired him to invent the cosmic ray neutron monitor that could better utilize the geomagnetic field as a magnetic spectrometer.

Within the same year, Simpson (1949b) had determined the relative production rate of neutrons when they interact in a various target or **producer**. He found that the production rate per unit mass of material is roughly proportional to $A^{0.4}$ where A is the atomic mass of the target. The choice of high atomic mass as the producer is preferred [Simpson et al. (1953)] because the number of produced neutrons increases with higher atomic mass of the producer.

Around 1952, Simpson had installed five monitoring stations (the first neutron monitor network) from the city of Chicago to the magnetic equator in Peru. This network allowed him to use the Earth's own magnetic field as an analyzer.

During 1954-55, the International Geophysical Year (IGY) which was at solar minimum, Rose et al. (1956) verified experimentally at sea-level that the neutron monitor responded to lower energy primary cosmic rays than muon detectors. The count rate at solar minimum is about $25,000 \text{ hr}^{-1}$.

Shortly afterward in 1957-58, the world-wide network of some fifty neutron monitoring stations was established.

In 1964, the IGY network was further supplemented with a second generation of monitors with the high counting rate of about $750,000 \text{ hr}^{-1}$ [Carmichael (1964)]. The new generation neutron monitor is called the **NM64**¹² while the original design is called the **IGY** monitor.

4.2 The Neutron Monitor Design

4.2.1 The IGY Monitor

The IGY monitor is the first generation of neutron monitor. Figure 4.1 represents an geometry base on earlier construction developed by the Chicago group [Simpson et al. (1953)]. This was chosen as the standard IGY because its construction was easy and from the fact that it could be readily extended in one direction without changing its response to the incident cosmic rays.

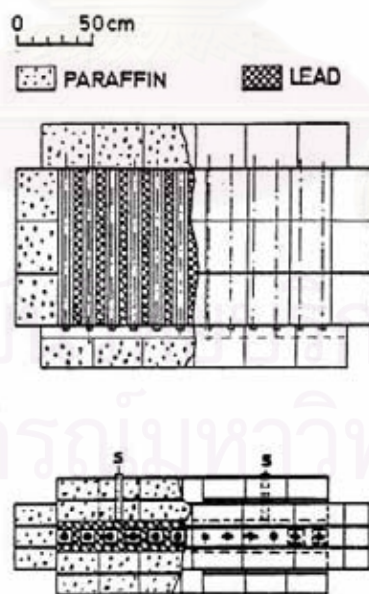
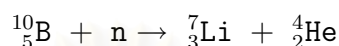


Figure 4.1: A standard 12-counter IGY neutron monitor [Simpson (1957)]. S are neutron source cavities

¹²NM64: NM is Neutron Monitor, and 64 is referred to year 1964 when the solar maximum and the new generation of neutron monitor was established.

The standard design uses BF₃ proportional counters with a diameter of 3.8 cm, an active length of 86.4 cm, and filled with BF₃ enriched to 96% ¹⁰B at 450 mm-Hg pressure. A slow neutron (considerably to be thermal energy) will be captured by a ¹⁰B nucleus and then induces the exothermic reaction:



This reaction is detailed in section 3.4: Slow Neutron Detection. Occurring radiations will be detected through ionizations they produce in the gas-filled chamber.

Surrounding each counter, there is an *inner moderator* with an average thickness of about 3.2 cm. The material used is paraffin which has the property of slowing down or moderating neutrons to near thermal environment to facilitate their capture in the BF₃ gas. Around the inner moderator, there is the producer in which the evaporation neutrons are produced following cosmic ray interactions. As the majority of the detected neutrons are produced in the immediate vicinity of the counter, the process is called **local neutron production**. All of the component is enclosed by a reflector, the function of which is to absorb and reflect unwanted low energy neutrons produced in the environment (or neutrons in background).

สถาบันวิทยบริการ
จุฬาลงกรณ์มหาวิทยาลัย

Table 4.1: Comparison between Standard IGY and NM64 Neutron Monitors.[†]

Specifications	Standard IGY	NM64
<i>Counters</i>		
Type	NW G-15-35A	BP28 or LND25373
Number per channel	12	6
Counter spacing (cm)	15.25	50
<i>Inner Moderator</i>		
Material	Paraffin	Low density polyethylene
Average thickness (cm)	3.2	2.0
<i>Producer</i>		
Material	Lead	Lead
Average depth (g/cm ²)	153	156
Projected top area per channel (m ²)	0.94	6.21
Length parallel to counters (m)	1.02	2.07
<i>Reflector</i>		
Material	Paraffin	Low density polyethylene
Average thickness (cm)	28	7.5
<i>Counting rate (1962)[‡]</i>		
of a high latitude sea-level station		
Per channel per hour	~12,000	~250,000
Per m ² of producer	~12,800	~ 40,000

[†] Source: Hatton (1971).

[‡] The counting rate in 1962 has been adopted as representative of the average counting rate over the solar cycle.

Table 4.2: Neutron Counters used in IGY and NM64 monitors.[†]

Specifications	NW G-15-35A	BP28	LND25373
Diameter (cm)	3.8	14.8	4.8
Length (cm)	87	191	191
Gas type	BF ₃ 96% ¹⁰ B	BF ₃ 96% ¹⁰ B	97% ³ He + 3%CO ₂
Pressure (mm-Hg)	450	200	3040
Thermal neutron absorption pathlength (cm)	18.2	41.0	1.9

[†] Source: Hatton (1971), Clem (2004; unpublished presentation document in 2004 ANNUAL CRONUS COLLABORATION MEETING).

4.2.2 The NM64 Monitor

The NM64 has been developed by Carmichael (1964), in order to increase counting rate and improve the statistical accuracy of neutron monitor data. Such an increase (to over an order of magnitude larger than the IGY monitor) could have been achieved at sea-level with the use of large (BP28¹³) BF₃ proportional counters developed at Chalk River by Fowler (1963). These BP28 counters have a diameter of 14.8 cm, an active length of 191 cm, and filled with BF₃ enriched to 96% ¹⁰B at 200 mm-Hg.

A NM64 monitor by Carmichael (1964) is shown in Figure 4.2, looked from top-view (above), and side-view (below). The design consists of 6 counters in each unit. Figure 4.3 represents the construction looked from the side-view.

An additional innovation in the NM64 monitor design was the use of low density polyethylene (instead of paraffin) as the moderator and reflector. The reason to use polyethylene is its ease manufactured which enabled the inner moderator and counter to be manufactured as a single assembly. Moreover, the flow properties of paraffin would result in deformation of the geometry with time whereas the polyethylene would not.

¹³The BP28 is manufactured in Canada by Electronic Associates Ltd. in their laboratories at 4616 Yonge St., Willowdale (Toronto), Ontario, to the design and specifications of the Chalk River Nuclear Laboratories, Atomic Energy of Canada Ltd.

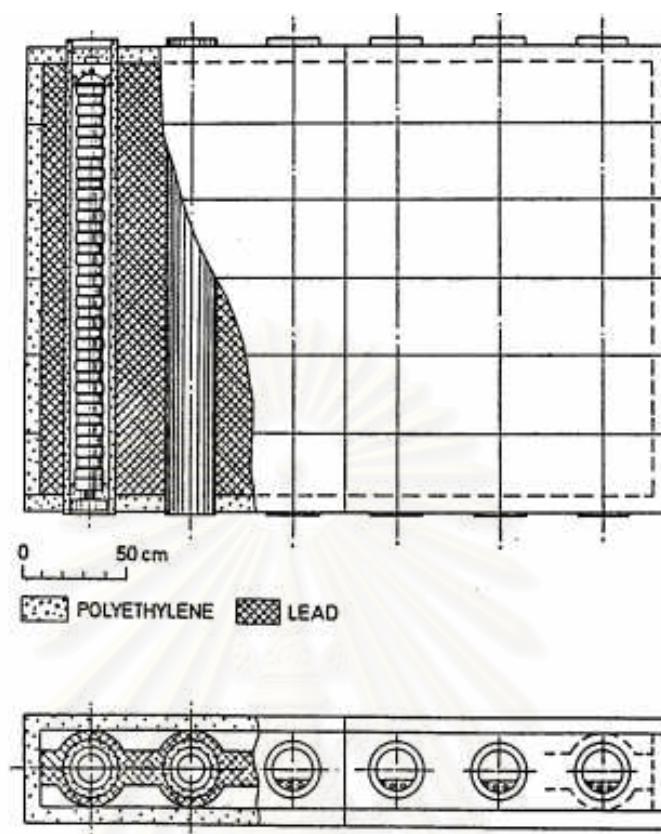
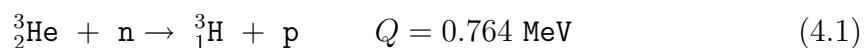


Figure 4.2: A 6-NM64 monitor [Carmichael (1964)].

A full-size NM64 neutron monitor consists of 18 counters in three independent units each containing 6 counters. The counting rate of an 18-NM64 is roughly 750,000 (three times from each unit counting rate) at a sea-level station with threshold rigidity less than 2 GV.

Another type of counter used for the NM64 is LND25373 with a smaller diameter of 4.8 cm, same active length of 191 cm. The gas filled in the chamber is the mixture of 97% ^3He and 3% CO_2 , and the pressure is 3,040 mm-Hg. A thermal neutron which is captured by a ^3He nucleus induces the exothermic reaction:



Details of the reaction have been discussed in section 3.4: Slow Neutron Detection.

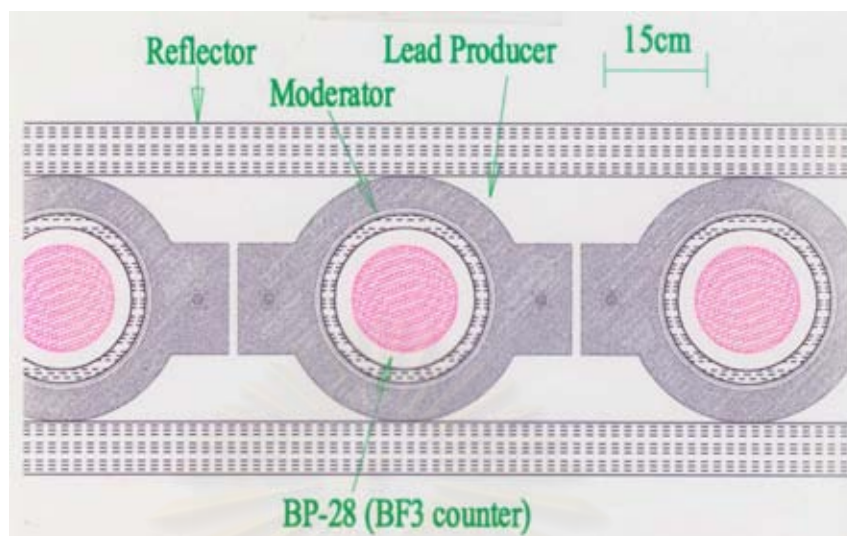


Figure 4.3: General geometry of NM64 monitors, represented in side-view. (Source: **Clem, John**, *Neutron Monitor Detection Efficiency*, unpublished presentation documents in 2004 ANNUAL CRONUS COLLABORATION MEETING.)

4.2.3 The Princess Sirindhorn Neutron Monitor

Owing to Princess Sirindhorn's graciousness, this neutron monitor station has been named **The Princess Sirindhorn Neutron Monitor**. The installation of the project is currently under operation (2004). Most equipments use material from the retired Morioka neutron monitor¹⁴ which has been donated by Shinshu University (Japan) under the support by US National Science Foundation and linked with Bartol Research Institute (University of Delaware, USA) for the transportation. In addition, in case of the installation, the research group at Delaware, Shinshu, University of Tasmania (Australia), Mahidol University (Thailand), have been consulted. Furthermore, the supplementary devices have been supported and funded by Ubol Ratchathani University (Thailand) and The Thailand Research Fund.

The specification of the detector has been presented in Table 4.3. Note that the size of the equipments has been determined at Chulalongkorn University

¹⁴The Morioka neutron monitor is the long-term cosmic ray monitor operated at Iwate University from 1970-1984. The original design is the IGY-type detector, but it was replaced with more sensitive NM64 detector tubes in 1977, which gradually increased in number until 1984 when 18 detector tubes began operated. After the retirement of Prof Chiba, the equipments were transferred ownership to Shinshu University in 2001.

(Thailand), the units are measured in inches.

Table 4.3: Specification of the Princess Sirindhorn Neutron Monitor.

<i>Counter</i> [†]	
Type	BP28 from Chalk River Lab. (Canada)
Filling	BF ₃ gas, 96% ¹⁰ B
Pressure	200 mm-Hg at 22°C
Diameter	5.785 to 6.03 inches (corrugated)
Overall Length	2.25 m (including electronics devices)
Active Length	1.90 m
Thermal Neutron	765 CPS/unit neutron flux
Sensitivity	
Resolution	12% Average FWHM for 2.3 MeV Peak
Background Counts	~4/minute
Operating Voltage	-2800 V
<i>Inner Moderator</i>	
Material	Polyethylene
Diameter	7.9 inches (20cm)
Thickness	0.8 inches (2 cm)
<i>Lead Producer</i>	
Thickness	2 inches
Height	14 inches
Width	19 inches
<i>Reflector</i>	
Material	Polyethylene
Thickness	3 inches

[†] Source: BP28 Chalk River Neutron Counter Operating Data.

Chapter 5

GEANT4

In this chapter, we introduce the software, called GEANT4, which is used as a simulation tool in our works. The scope of this chapter is to:

- introduce a concept of the simple main program.
- provide a description of the principle routine implemented in the main program.

GEANT4 (Geometry and Tracking 4) is a toolkit for the simulation of the passage of particle through matter. It has been developed and maintained by a world-wide collaboration of approximately 100 scientists around the world. This is supported and has a center at CERN.¹⁵

GEANT4 (or G4) is the fourth¹⁶ version and based on C++ language which supports object oriented programming; the function enables further development and easily design. The version we used is G4.6.1 while a current version (December, 2004) is G4.6.2 with a little change of some details in library source.

5.1 The *main()* Method

In order to do a simulation, the *main()* program must be executed. The contents of *main()* will vary according to the needs of a given simulation application and therefore must be supplied by the user. The GEANT4 toolkit does not provide a *main()* program, so that the user has to build it by including sub-programs needed to run the application. The source listing 5.1 provided here is the simplest example of *main()* required to build a simulation program. This

¹⁵CERN (Conseil Européen pour la Recherche Nucléaire; French words) is the European Organization for Nuclear Research, the world's largest particle physics center. The organization locates cover area in three countries, Switzerland, France, and Italy. The facilities from CERN have been used by scientists and students in approximately 220 institutes and universities.

¹⁶The previous (third) version is based on FORTRAN language.

example is from the first novice example stored at `example/novice/N01`.

Source listing 5.1: A sample *main()* program.

```

1 #include "G4RunManager.hh"
2 #include "G4UImanager.hh"

3 #include "ExN01DetectorConstruction.hh"
4 #include "ExN01PhysicsList.hh"
5 #include "ExN01PrimaryGeneratorAction.hh"

6 int main()
7 {
8     // construct the default run manager
9     G4RunManager* runManager = new G4RunManager;

10    // set mandatory initialization classes
11    runManager->SetUserInitialization(new ExN01DetectorConstruction);
12    runManager->SetUserInitialization(new ExN01PhysicsList);

13    // set mandatory user action class
14    runManager->SetUserAction(new ExN01PrimaryGeneratorAction);

15    // initialize G4 kernel
16    runManager->initialize();

17    // get the pointer to the UI manager and set verbosity
18    G4UImanager* UI = G4UImanager::GetUIpointer();
19    UI->ApplyCommand("/run/verbose 1");
20    UI->ApplyCommand("/event/verbose 1");
21    UI->ApplyCommand("/tracking/verbose 1");

22    // start a run
23    int numberOfEvent = 3;
24    runManager->BeamOn(numberOfEvent);

25    // job termination
26    delete runManager;
27    return 0;
28 }

```

The *main()* program is implemented by two toolkit classes, *G4RunManager* and *G4UImanager* (in the two first lines), and three classes in the following lines,

ExN01DetectorConstruction, *ExN01PhysicsList* and *ExN01PrimaryGeneratorAction*, which are derived from toolkit classes. Each of these are explained in the following subsections.

5.1.1 G4RunManager

The first thing *main()* must do is create an instance of the *G4RunManager* class. This is the only manager class in the GEANT4 kernel which should be explicitly constructed in the user's *main()*. It controls the flow of the program and manages the event loop(s) within a run. When *G4RunManager* is created, the other major manager classes are also created. They are deleted automatically when *G4RunManager* is deleted. The run manager is also responsible for managing initialization procedures, including methods in the user initialization classes. Through these the run manager must be given all the information necessary to build and run the simulation, including

- how the detector should be constructed,
- all the particles and all the physics processes to be simulated,
- how the primary particle(s) in an event should be produced and
- any additional requirements of the simulation.

In the sample *main()* the 11th and 12th lines

```
runManager->SetUserInitialization(new ExN01DetectorConstruction);
runManager->SetUserInitialization(new ExN01PhysicsList);
```

create objects which specify the detector geometry and physics processes, respectively, and pass their pointers to the run manager.

ExN01DetectorConstruction is a user initialization class (which is derived from *G4VUserDetectorConstruction*). This is where the user describes the entire detector setup, including

- its geometry,

- the materials used in its construction,
- a definition of its sensitive regions and
- the readout schemes of the sensitive regions.

Similarly *ExN01PhysicsList* is derived from *G4VUserPhysicsList*. This class requires the user to define

- the particles to be used in the simulation,
- the range cuts for these particles and
- all the physics processes to be simulated.

The next instruction at the 14th line in *main()*

```
runManager->SetUserAction(new ExN01PrimaryGeneratorAction);
```

creates an instance of a particle generator and passes its pointer to the run manager. *ExN01PrimaryGeneratorAction* is an example of a user action class (which is derived from *G4VUserPrimaryGeneratorAction*). In this class the user must describe the initial state of the primary event. This class has a public virtual method named *generatePrimaries()* which will be invoked at the beginning of each event. Note that GEANT4 does not provide any default behavior for generating a primary event.

The next instruction at the 16th line

```
runManager->initialize();
```

performs the detector construction, creates the physics processes, calculates cross sections and otherwise sets up the run.

At the 23th and 24th lines, the final run manager method in *main()*

```
int numberOfEvent = 3;
```

```
runManager->beamOn(numberOfEvent);
```

begins a run of three sequentially processed events. The *beamOn()* method may be invoked any number of times within *main()* with each invocation representing a separate run. Once a run has begun neither the detector setup nor the physics processes may be changed. However, they may be changed between runs.

At the 18th line, the command

```
G4UImanager* UI = G4UImanager::getUIpointer();
```

creates a pointer to the interface manager. This manager class is created when the run manager is created. The pointer *UI* is created in order for the user to issue commands to the program. In the present example the *applyCommand()* method is called three times to direct the program to print out information at the run, event and tracking levels of simulation. A wide range of commands is available which allows the user detailed control of the simulation.

5.2 User Initialization and Action Classes

Mandatory User Classes

Source listing 5.1 presents the simplest example for the *main()* program. In any *main()* program, there are at least 3 classes which must be defined by the user. Two of them are **user initialization classes**, and the other is a **user action class**. From source listing 5.1, these three classes are

- *ExN01DetectorConstruction*,
- *ExN01PhysicsList* and
- *ExN01PrimaryGeneratorAction*.

The first two classes are the user initialization classes. They must be derived from the abstract base classes provided by GEANT4: *G4VUserDetectorConstruction*, *G4VuserPhysicsList*, respectively. The last one is the user action class which must be derived from *G4VUserPrimaryGeneratorAction*.

As mentioned in the previous subsection, *G4VUserDetectorConstruction* requires the user to define the **detector** and *G4VUserPhysicsList* requires the user to define the **physics**. Detector and physics definition will be discussed later.

Optional User Action Classes

In addition, GEANT4 also provides 5 optional user action classes:

- *G4UserRunAction*
- *G4UserEventAction*
- *G4UserStackingAction*
- *G4UserTrackingAction*
- *G4UserSteppingAction*

5.2.1 G4UserRunAction

This is the base class of a user's action class from which you can derive your own concrete class. It defines the user's action at the beginning and the end of each run. This base class has two virtual methods, as follows:

beginOfRunAction(const G4Run)*

This method is invoked at the beginning of the *beamOn()* method but after confirmation of the conditions of the GEANT4 kernel. Presumable uses of this method are:

- set a run identification number,
- book histograms, and
- set run specific conditions of the sensitive detectors and/or digitizer modules (e.g., dead channel).

endOfRunAction(const G4Run)*

This method is invoked at the very end of the *beamOn()* method. Typical use cases of this method are

- store/print histograms and
- manipulate run summaries.

5.2.2 G4UserEventAction

This class has two virtual methods which are invoked for each event and which can be implemented by the user.

beginOfEventAction(const G4Event)*

This method is invoked before converting the primary particles to *G4Track* objects. Typical use cases of this method are:

- event selection and
- define histograms.

endOfEventAction(const G4Event)*

This method is invoked at the very end of the event processing. It is used to

- analyze the current event.

5.2.3 G4UserStackingAction

This class has three virtual methods which are:

PrepareNewEvent()

- Reset priority control.

ClassifyNewTrack(const G4Track)*

- Invoked every time a new track is pushed.
- Classify a new track; priority control

- *Urgent, Waiting, PostponeToNextEvent, Kill.*

NewStage()

- Invoked when the *Urgent* stack becomes empty.
- Change the classification criteria.
- Event filtering (Event abortion).

5.2.4 G4UserTrackingAction

This class has two virtual method, which are:

PreUserTrackingAction(const G4Track)*

- Decide trajectory should be stored or not.
- Create user-defined trajectory.

PostUserTrackingAction(const G4Track)*

5.2.5 G4UserSteppingAction

This class must be inherited by the user in order to have the possibility of intervening after a stem has been undertaken. An object of the class that the user implements must be passed to the run manager by invoking *SetUserAction* in the *main()* method. There is a method which the user must implemented:

void UserSteppingAction(Const G4Step)*

- This will be invoked step by step during tracking.
- The pointer to an object of type *G4Step* provides (hopefully) enough information to allow the user to retrieve any information he/she might need.

5.3 Detector Geometry

A detector geometry in GEANT4 is made of a number of volumes. The largest volume is called the **World** volume. It must contain, with some margin, all other volumes in the detector geometry. The other volumes are created and placed inside previous volumes, included in the World volume. The most simple (and efficient) shape to describe the World is a box.

Each volume is created by describing its shape and its physical characteristics, and then placing it inside a containing volume.

When a volume is placed within another volume, we call the former volume, the daughter volume, and the latter the mother volume. The coordinate

system used to specify where the daughter volume is placed, is the coordinate system of the mother volume.

In GEANT4, volumes cannot overlap, but we can use boolean operations to combine complicated volumes. To have a volume implemented in the GEANT4, one has to go through 4 steps.

1. Create a solid.
 - Define shape and size of the solid.
2. Define a material.
 - Specify its attributes.
3. Create a logical volume.
 - Use the created solid.
 - Add the defined material.
4. Create a physical volume.
 - Use the logical volume to place into the specific location.

5.3.1 Create a Solid

A solid describes a shape of a volume. A solid is a geometrical object that has a shape and specify values for each of that shape's dimensions.

To create a simple box, one has simply to define its name and its dimensions along each cartesian axes. In *Novice Example N01*, there is a box definition in the source file *ExN01DetectorConstruction.cc*, as listed in the source listing 5.2.

Source listing 5.2: Creating a box.

```

#include "G4Box.hh"
...

G4double expHall_x = 3.0*m;
G4double expHall_y = 1.0*m;
G4double expHall_z = 1.0*m;

G4Box* experimentalHall_box
    = new G4Box( name = "expHall_box", expHall_x, expHall_y, expHall_z );

```

This creates a box named "*expHall_box*" with extent from -3.0 meters to +3.0 meters along the *X* axis, from -1.0 to 1.0 meters in *Y*, and from -1.0 to 1.0 meters in *Z*.

To create a simple cylinder, one can use the *G4Tubs* class as shown in source listing 5.3.

Source listing 5.3: Creating a cylinder.

```

#include "G4Tubs.hh"
...

G4double innerRadiusOfTheTube = 0.*cm;
G4double outerRadiusOfTheTube = 60.*cm;
G4double hightOfTheTube = 25.*cm;
G4double startAngleOfTheTube = 0.*deg;
G4double spanningAngleOfTheTube = 360.*deg;

G4Tubs* tracker_tube
    = new G4Tubs( name = "tracker_tube",
                 innerRadiusOfTheTube,
                 outerRadiusOfTheTube,
                 hightOfTheTube,
                 startAngleOfTheTube,
                 spanningAngleOfTheTube);

```

This creates a full cylinder, named "*tracker_tube*", of radius 60 cm and length 50 cm.

5.3.2 Define a Material

In nature, general materials (chemical compounds, mixtures) are made of elements, and elements are made of isotopes. Therefore, these are the three main classes designed in GEANT4; *G4Element*, *G4Material*, and *G4Isotope*. Each of these classes has a table as a static data member, which is for keeping track of the instances created of the respective classes.

The *G4Element* class describes the properties of the atoms:

- atomic number,
- number of nucleons,
- atomic mass,
- shell energy,
- as well as quantities such as cross sections per atom, etc

The *G4Material* class describes the macroscopic properties of matter:

- density, state,
- temperature, pressure,
- as well as macroscopic quantities like radiation length, mean free path, dE/dx , etc.

Source listing 5.4 is an example of creating a water molecule (by defining its molecular components) and air molecule (by defining the fractional mass of its components), respectively.

Source listing 5.4: Creating water and air molecule.

```

a = 1.01*g/mole;
G4Element* elH = new G4Element(name = "Hydrogen", symbol="H" , z= 1., a);

a = 14.01*g/mole;
G4Element* elN = new G4Element(name = "Nitrogen", symbol="N" , z= 7., a);

a = 16.00*g/mole;
G4Element* elO = new G4Element(name = "Oxygen" , symbol="O" , z=8. , a);

density = 1.000*g/cm3;
G4Material* H2O = new G4Material(name="Water", density, ncomponents = 2);
  H2O->AddElement(elH, natoms = 2);
  H2O->AddElement(elO, natoms = 1);

density = 1.290*mg/cm3;
G4Material* Air = new G4Material(name = "Air", density, ncomponents = 2);
  Air->AddElement(elN, fractionmass = 70*perCent);
  Air->AddElement(elO, fractionmass = 30*perCent);

```

5.3.3 Create a Logical Volume

To create a logical volume, one must start with a solid and a material. So, using the box created before, one can create a simple logical volume filled with argon gas (see *ExN01DetectorConstruction.cc*) by entering:

```

G4LogicalVolume* experimentalHall_log
  = new G4LogicalVolume(experimentalHall_box, Ar, name = "expHall_log");

```

5.3.4 Create a Physical Volume

To place a volume, we start with a logical volume, and then we decide the already existing volume inside of which to place it. Then we decide where to place its center within that volume, and how to rotate it. Once we have made these decisions, we can create a physical volume, which is the placed instance of the volume, and embodies all of these attributes. Source listing 5.5 is an example of defining a simple physical volume.

Source listing 5.5: A simple physical volume.

```

G4double trackerPos_x = -1.0*meter;
G4double trackerPos_y = 0.0*meter;
G4double trackerPos_z = 0.0*meter;

G4VPhysicalVolume* tracker_phys
= new G4PVPlacement(0,                // no rotation
                   G4ThreeVector(trackerPos_x, trackerPos_y, trackerPos_z),
                                     // translation position
                   tracker_log,      // its logical volume
                   "tracker",        // its name
                   experimentalHall_log, // its mother (logical) volume
                   false,            // no boolean operations
                   0);               // its copy number

```

This places the logical volume *tracker_log* at the origin of the mother volume *experimentalHall_log*, shifted by one meter along *X* and unrotated. The resulting physical volume is named “*tracker*” and has a copy number of 0.

An exception exists to the rule that a physical volume must be placed inside a mother volume. That exception is for the World volume, which is the largest volume created, and which contains all other volumes. This volume obviously cannot be contained in any other. Instead, it must be created as a *G4PVPlacement* with a *null mother pointer*. It also must be unrotated, and it must be placed at the origin of the global coordinate system.

5.4 Particles and Physics Processes

To do a simulation with GEANT4, the user must specify particles and physics processes by deriving his/her own class from *G4VuserPhysicsList*. This class has three virtual methods:

- *ConstructParticle()*: construction of particles
- *ConstructProcess()*: construct processes and register them to particles
- *SetCuts()*: setting a range cut value for all particles

5.4.1 Particle Definition

GEANT4 provides various types of particles for use in simulations. Each particle is represented by its own class, which is derived from *G4ParticleDefinition*. This class contains properties which characterize individual particles such as name, mass, charge, spin, and so on. These attributes are read-only and cannot be changed without re-building the libraries. Particles are organized into six major categories:

- lepton,
- meson,
- baryon,
- boson,
- shortlived, and
- ion.

Constructing Particles

The *ConstructParticle()* from *G4VUserPhysicsList* must be implemented by the user in order to create all particles which are needed in the simulation (both primary particles and secondary products which are generated by physics processes the user uses).

For example, suppose we need a proton and a geantino, the *ConstructParticle()* method is implemented as shown in source listing 5.6.

Source listing 5.6: Construct a proton and a geantino.

```
void ExN01PhysicsList::ConstructParticle()
{
    G4Proton::ProtonDefinition();
    G4Geantino::GeantinoDefinition();
}
```

Note that a geantino is a virtual particle used for simulation. It does not interact with materials. It is used for a geometrical probe when it transports through regions in the detector.

5.4.2 Physics Processes

Physics processes describe the interaction of particles with matter. In GEANT4, there are 7 major categories of physics process:

- transportation,
- electromagnetic,
- hadronic,
- decay,
- optical,
- photolepton_hadron, and
- parameterisation.

Constructing Processes

ConstructProcess() is a pure virtual method which is used to construct physics processes and register them to particles. Source listing 5.7 is an example of electromagnetic process registration for photons.

Source listing 5.7: Register processes for a photon.

```

void MyPhysicsList::ConstructProcess()
{
    // Define transportation process
    AddTransportation();
    // electromagnetic processes
    ConstructEM();
}
void MyPhysicsList::ConstructEM()
{
    // Get the process manager for gamma
    G4ParticleDefinition* particle = G4Gamma::GammaDefinition();
    G4ProcessManager* pmanager = particle->GetProcessManager();

    // Construct processes for gamma
    G4PhotoElectricEffect * thePhotoElectricEffect = new G4PhotoElectricEffect();
    G4ComptonScattering * theComptonScattering = new G4ComptonScattering();
    G4GammaConversion* theGammaConversion = new G4GammaConversion();

    // Register processes to gamma's process manager
    pmanager->AddDiscreteProcess(thePhotoElectricEffect);
    pmanager->AddDiscreteProcess(theComptonScattering);
    pmanager->AddDiscreteProcess(theGammaConversion);
}

```

5.5 Run and Event

5.5.1 Run

As an analogy of the real experiment, a Run of GEANT4 starts with “*Beam On*”. The Run is the largest unit of simulation and consists of a series of events. Within a run, the setup of

- detector geometry,
- sensitive detectors, and
- physics processes

cannot be modified. A Run is represented by an object of the *G4Run* class and begins when the *beamOn()* method of the *G4RunManager* class is invoked.

G4Run

G4Run contains a Run identification number (which should be set by the user) and the number of events to be simulated during that Run.

The Run identification number is not used by the GEANT4 kernel and it is then an arbitrary number which is provided for the convenience of the user.

G4Run contains pointers to the name tables of *G4VHitsCollection*'s and *G4VDigiCollection*'s which are associated in case *Sensitive Detectors* and *Digitizers* are implemented.

G4RunManager

As mentioned in section 5.1.1, the *G4RunManager* class manages the procedures of a Run. In its constructor, all the GEANT4 manager classes are constructed. These managers are then deleted in its destructor.

In addition, *G4RunManager* is a *singleton*; only one run manager can exist throughout the whole program. A pointer to this object can be obtained by invoking the *G4RunManager*'s method; *GetRunManager()*.

All user initialization classes and user action classes should be assigned to *G4RunManager* before the initialization of the GEANT4 kernel by using the *SetUserInitialization()* and the *SetUserAction()* methods. The information on *G4RunManager*, can be found in “GEANT4 User’s Guide” and “Software Reference Manual” at <http://geant4.web.cern.ch/geant4/>.

5.5.2 Event

At beginning of processing, an event contains primary particles. These primaries are pushed into a stack. When the stack becomes empty, processing of an event is over.

An event in GEANT4 is represented by the class *G4Event*, which contains all quantities needed to characterize the simulated event. At the end of its processing, it has following objects:

- list of Primary vertexes and particles,
- trajectory collection (optional),
- hits collections, and
- digits collections (optional).

5.6 Physics List Package

In our simulation, we included a package of physics lists downloaded from <http://cmsdoc.cern.ch/~hpw/GHAD/HomePage/>.

The package we used is LHEP_PRECO_HP. This package includes physics lists for low energy dosimetric applications with neutrons.

This package uses a pre-equilibrium decay model for modeling the inelastic interactions of neutrons (and protons). It uses the *Wellisch-Axen* systematics for cross-section calculation of nucleon nuclear reaction cross-sections in the giant resonance region. Point-wise evaluated cross-section data are used to model neutron interactions from thermal energies to ~ 20 MeV. This applies to capture, elastic scattering, fission and inelastic scattering processes. For the information on LHEP_PRECO_HP, please see the website.

Chapter 6

Simulations, Results and Discussions

In this chapter, we present results from the simulation using GEANT4 software. In the simulations, we constructed the geometry and material obtained from the Princess Sirindhorn neutron monitor¹⁷ which will be installed at Doi Inthanon, Chiang Mai province. This detector is the NM64 type with the counter type BP-28.

6.1 The Working Procedure

In our works, the working procedure may be divided into 6 steps, which are:

1. Construct the geometry
2. Setup kinematics
 - Directions and position of the incoming particles
3. Construct physics processes
 - Choose suitable physics processes.
4. Construct recording process
5. Run and record data
6. Analysis

The first step in our work is to construct the detector geometry. The material of the detector must be defined and we have to check the declaration of the material by determining its physics processes because some of declaration might not work properly. The specification of the detector components, i.e., shape, size, placement, have to be checked in visualization mode.

¹⁷The process of installation is under operation (now in 2004).

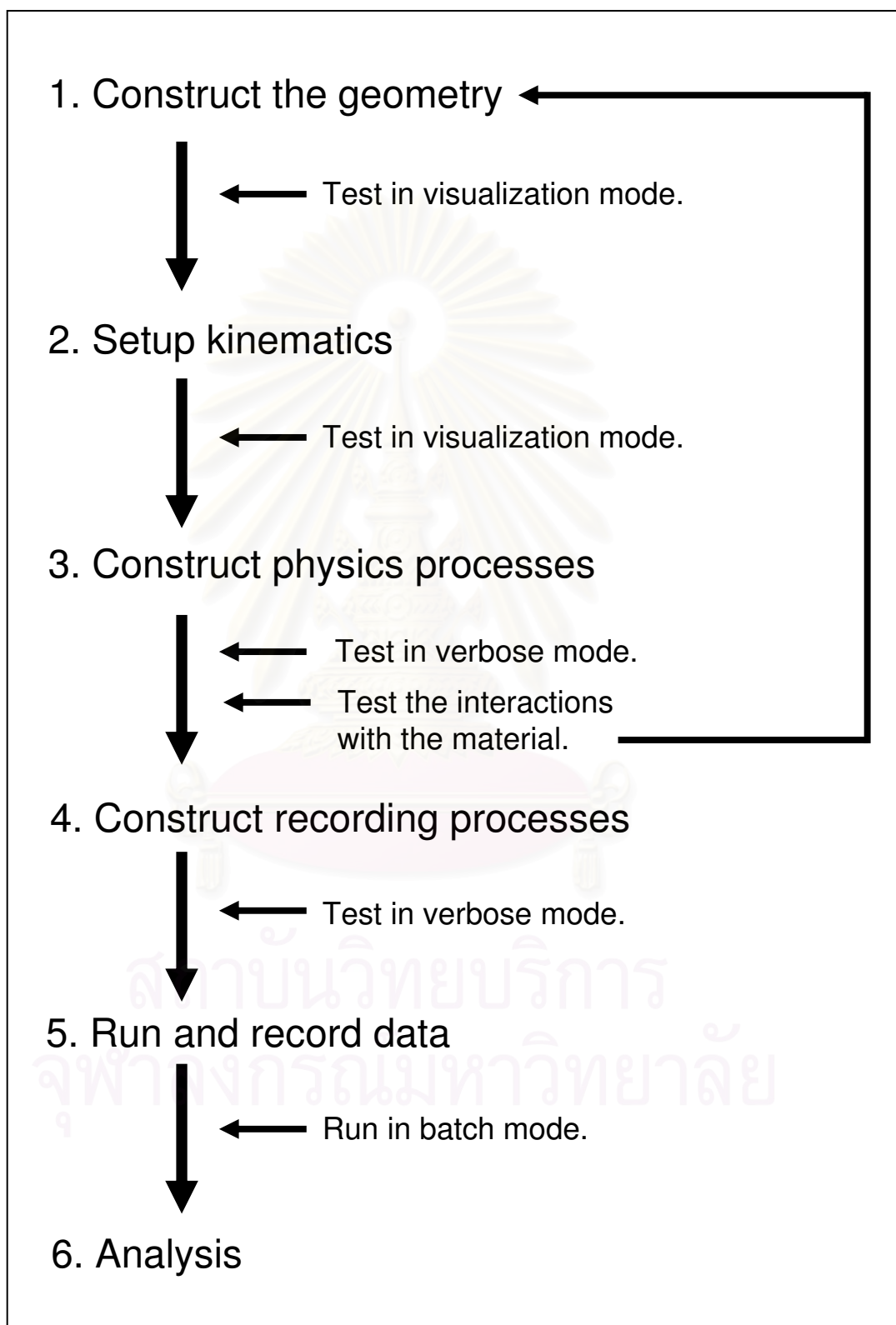


Figure 6.1: The working procedure.

The second step is the setup of the kinematics. At this step, we set the direction and the position of the incoming beam. This step was tested in visualization mode.

At the third step, the physics processes needed to use in the simulations are constructed. This step took a long time in order to choose suitable processes and there were many problems, e.g., bugs in the codes, limitation of the chosen processes, etc. This step, for convenience, is displayed and tested in text mode.

The fourth step is to construct the recording process. In this step we built or modified classes (from the GEANT4 examples) to record the data from generated events. Many files were implemented in the program and the program became more complicated.

The fifth step is running and recording data. This step took several minutes to many days depending on aspect of the simulation. The batch mode was set during simulations.

The last step is the analysis process. After we obtained data from the simulation in the previous steps, we had to interpret data using graphs or histograms and used concepts in physics to explain the results.

6.2 The Geometry

To do a simulation, first we have to construct the geometry of the neutron monitor. The geometry and material used in the simulation are modeled from the Princess Sirindhorn neutron monitor. However, some geometric parameters are somewhat different from the detector specification since we initially obtained these parameters by estimation. The differences between the specification and parameter used in simulation are compared in Table 6.1. Although the differences affects to the number of neutron counts, the physics inside the detector does not change. The general construction of the neutron monitor used in the simulation

is presented in Figure 6.2.

Table 6.1: Differences parameter from specification and used in simulations.

	Specification	Simulation
<i>Counter</i>		
Active length	1.9 m	2.3 m
Shape	Corrugated	Cylinder
Diameter	5.8 to 6.3 inches	8 inches
<i>Inner moderator</i>		
Thickness	0.8 inches	1.0 inch

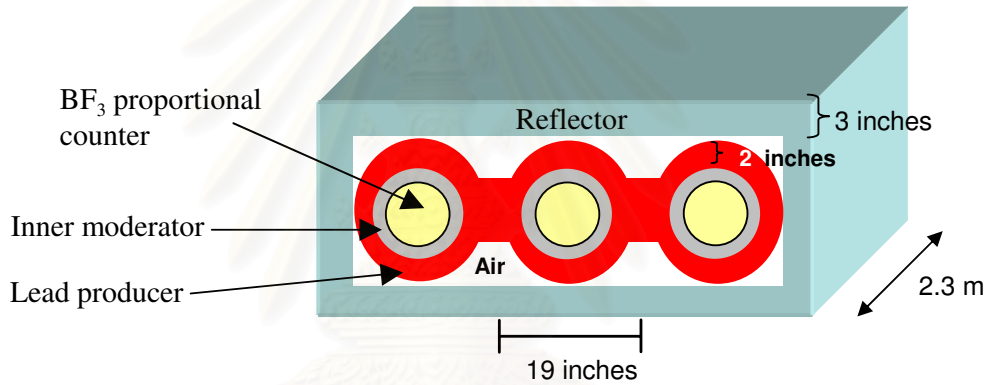


Figure 6.2: A 3-Tube NM64 geometry.

Figure 6.2 illustrates side view of a 3-Tube NM64. This prototype has three proportional counters filled with BF_3 enriched to 96% ^{10}B at 200 mm-Hg pressure. The counter has a diameter of 8 inches, an overall length of 2.30 m. Surrounding each counter, there is an inner moderator with a thickness of about 1 inch. The material is low density polyethylene. Around the inner moderator, there is a lead producer with a thickness of about 2 inches. All of the component is enclosed by a reflector made of low density polyethylene with a thickness of about 3 inches.

In fact, we ignore the electronics devices and the container (made of thin stainless metal) of the proportional counter in the simulation geometry. The effects from these omitted devices may be for the future study.

6.3 The Proportional Counter

As described in section 3.5, a proportional counter is used for detecting the deposited energy from the charged radiation passing through the gas chamber. Even though neutrons do not leave an ion trail in the proportional tube, the absorption of a neutron by a target nucleus is usually followed by the emission of charged particles which can be detected. A proportional tube filled with BF_3 gas responds to neutrons by the exothermic reaction $^{10}\text{B}(n,\alpha)^7\text{Li}$. The reaction cross-section is inversely proportional to the neutron velocity, having a thermal endpoint of 3,840 barns as shown in Figure 3.5. Details of the reaction have been discussed in section 3.4.

From the reaction, a thermal neutron is captured and then ^7Li with α are released. Because of the conservation of momentum, and since the neutron has very little momentum, the outgoing radiations move in opposite direction (see Figure 6.3).

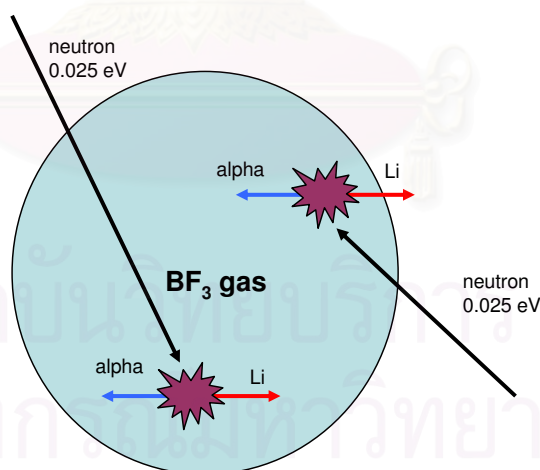


Figure 6.3: Neutron capture events in a BF_3 proportional chamber.

The energy deposited in the gas chamber depends on the location of the absorption event. By ionization loss, the outgoing radiations need sufficient distance to deposit their entire energy; called **ionization path length**. If the size of the tube is not large compare to the ionization path length of the products

or if the reaction occurs near the wall boundaries, some of the reactions will no longer deposit their entire energy into the detector. If either product hits the wall some of the energy escapes the detector and a smaller pulse is produced as shown in Figure 6.4. This feature in energy distribution is called the **wall effect**. In addition, the gas density also affects the ionization path length which results in the deposition of energy in the chamber.

Figure 6.4 shows a typical energy distribution produced by a neutron source in a BP-28 Chalk River Neutron Counter. The plot is obtained from the *NM-64 Neutron Monitor Specification Data Sheet*. This plot from a neutron source is similar to the energy distribution in Figure 6.5 and Figure 6.6.

Figure 6.5 shows a typical spectrum from a bare BP-28 counter enclosed by a 0.8 cm thickness inner moderator (which is used in the Princess Sirindhorn Neutron Monitor). The experiments have been taken in 2004 at Chulalongkorn University. This graph was obtained from collected signal counts for a period of about 15 days. The horizontal axis represents channel of the counter, which relates to energy deposit in the gas filled chamber.

Figure 6.6 represents spectra from four selected counters in the Newark Neutron Monitor (Australia) by the Bartol Research Group¹⁸. The data has been collected in July, 1st 2004.

From Figure 6.4, Figure 6.5 and Figure 6.6, we can see that the trend of the graphs seem well corresponded. There are two peaks, the higher one is referred to the major channel from the neutron capture (94% probabilities), while the other one is referred to ground state process of about 6% probabilities (see section 3.4). Furthermore, we can obviously see the wall effect at the left of all curves.

In case of the simulation, there is a difficulty about the density of the BF_3 gas in the chamber. It is an unknown parameter which we cannot get from

¹⁸The data had been acquired by private communications.

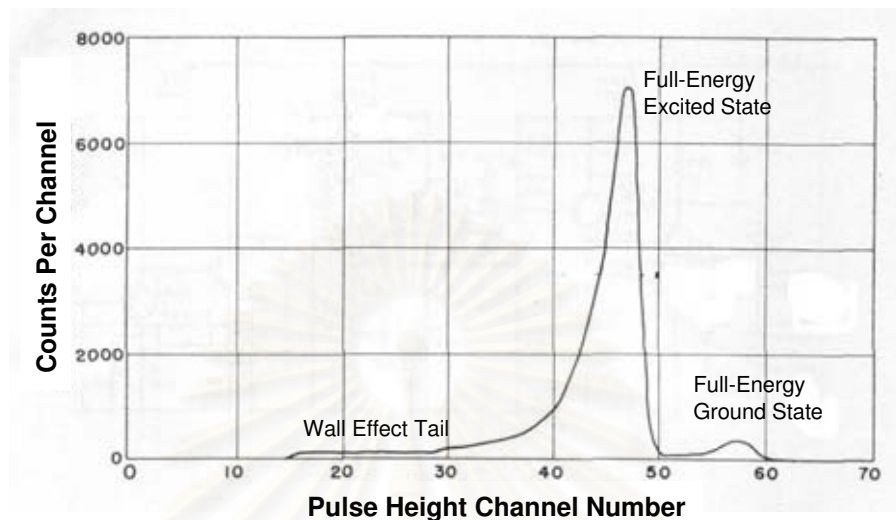


Figure 6.4: Energy distribution produced by a neutron source in a PB-28 Chalk River Neutron Counter. The plot is acquired from the *NM-64 Neutron Monitor Specification Data Sheet*.

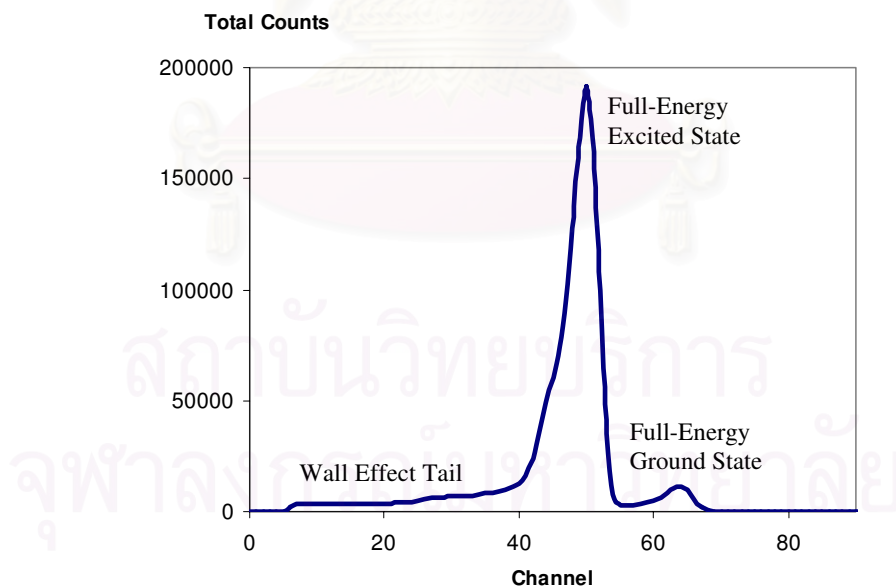


Figure 6.5: Energy spectrum from signal probes of a bare BP-28 counter (which will be set up for the Princess Sirindhorn Neutron Monitor). The counts have been collected for a period of about 15 days in 2004 at Chulalongkorn University. (Courtesy of Alejandro Saiz.)

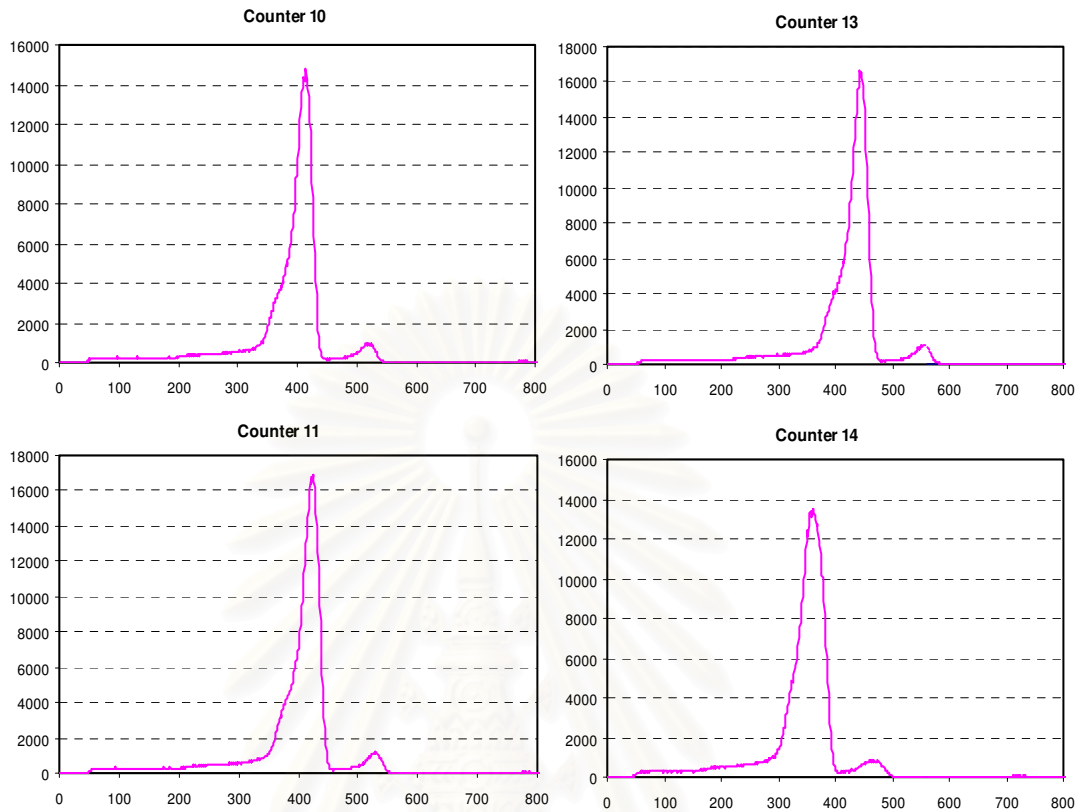


Figure 6.6: Energy spectrum from four selected counters in the Newark Neutron Monitor at Australia. The data has been taken in July, 1st 2004.

the specification of the BP-28 counter. This is important because density affects the cross-section and also to the wall effect. One way to expect it is using the ideal gas formula,

$$pV = nRT, \quad (6.1)$$

where p is gas pressure, V is volume of the gas container, n is number of moles, R is universal gas constant (8.31 J/mol·K), T is temperature. This equation is applicable to any pure gas system with low pressure and high temperature. The pressure in the gas chamber is considerably low at 200 mm-Hg while it is placed in the room temperature, which is not adapted to the use of the ideal gas formula. Nevertheless, we might use it to roughly predict the gas density. From calculations, we use

$$p = \frac{200}{760} \times 1.013 \times 10^5 \text{ N/m}^2,$$

$$T = 300 \text{ K},$$

and the molar mass of BF_3 is 67.8 g/mol, and finally found that the density is about 0.72 kg/m³. Note that in preliminary calculation, we applied the molar mass of BF_3 at 63.6 g/mol. So we have got the density about 0.68 kg/m³, which has been used in the following simulation. However, this is not a vital important to us since the gas does not act as a perfect ideal gas. The calculation is a guideline to roughly estimate the value of the parameter applied in the simulation.

Simulation I: Energy distribution from the $^{10}\text{B}(\text{n},\alpha)^7\text{Li}$ reaction.

The goal is to simulate the $^{10}\text{B}(\text{n},\alpha)^7\text{Li}$ event in the BF_3 proportional counter compare the results for various gas densities.

In this simulation, we shoot thermal neutrons into the BF_3 chamber for various gas densities. These neutrons will be captured by ^{10}B target nucleus and induce exothermic reaction $^{10}\text{B}(\text{n},\alpha)^7\text{Li}$. The products will deposit their energy in the gas chamber, although a 0.48-MeV gamma emission from excited ^7Li does not leave any significant in the gas chamber but it may sometimes undergo Compton scattering with electron resulting in recoil electron. If the electrons occur in the gas chamber, they produce small pulse which is illustrated in Figure 6.7.

Figure 6.7 displays energy distribution from a BF_3 neutron counter. These are from simulation using GEANT4 with gas density (a,b) 0.1 kg/m³, (c,d) 0.68 kg/m³, and (e,f) 2.0 kg/m³. The initial neutrons (100,000 events) were shot at the center of the BF_3 chamber with thermal energy (0.025 eV). The roughly stopping path length in BF_3 chamber for each case are shown in Table 6.2. The bin size of the histograms is 0.2 MeV/bin. The wall effect begins at 0.83 MeV and two full-energy peaks are at 2.27 and 2.75 MeV.

Table 6.2: The stopping path length in BF_3 chamber.

Gas density	${}^7\text{Li}$	α
0.1 kg/m^3	9.0 cm	7.5 cm
0.68 kg/m^3	1.5 cm	1.3 cm
2.0 kg/m^3	4.48 mm	4.5 mm

Figure 6.8 displays the energy distribution from electrons produced by the Compton scattering of a 0.48-MeV gamma (left panel), and (right panel) the plots of Compton scattering probabilities versus gas density. In the simulation, a million of 0.48 MeV gammas were shot at the center of gas chamber with various densities.

Discussion

These results imply that the density parameter or grammage has an obvious effect to the energy distribution. From Figure 6.7 in the left panel, at low grammage, the wall effect tail is obviously seen. At higher grammage, however, the wall effect tail is reduced.

Since the proportional counter has a diameter of about 19 cm (in our simulation), the use of gas density as 2.0 kg/m^3 -which has the stopping path length of the charged radiations in scale of mm, seem unlikely.

From Figure 6.8 we found that the Compton scattering probabilities in the gas chamber relate directly to the grammage and the energy distribution becomes wider with more grammage.

From the simulation, we found that no matter how we vary the density, we always get the same full energy peaks but different wall effect tail. We conclude that the values of the gas density as 0.68 kg/m^3 (from calculations) may be acceptable to use in the simulation.

In comparison between the experiment (Figure 6.5 and Figure 6.6) and the simulation (Figure 6.7), both are well consistent, but the simulation provides

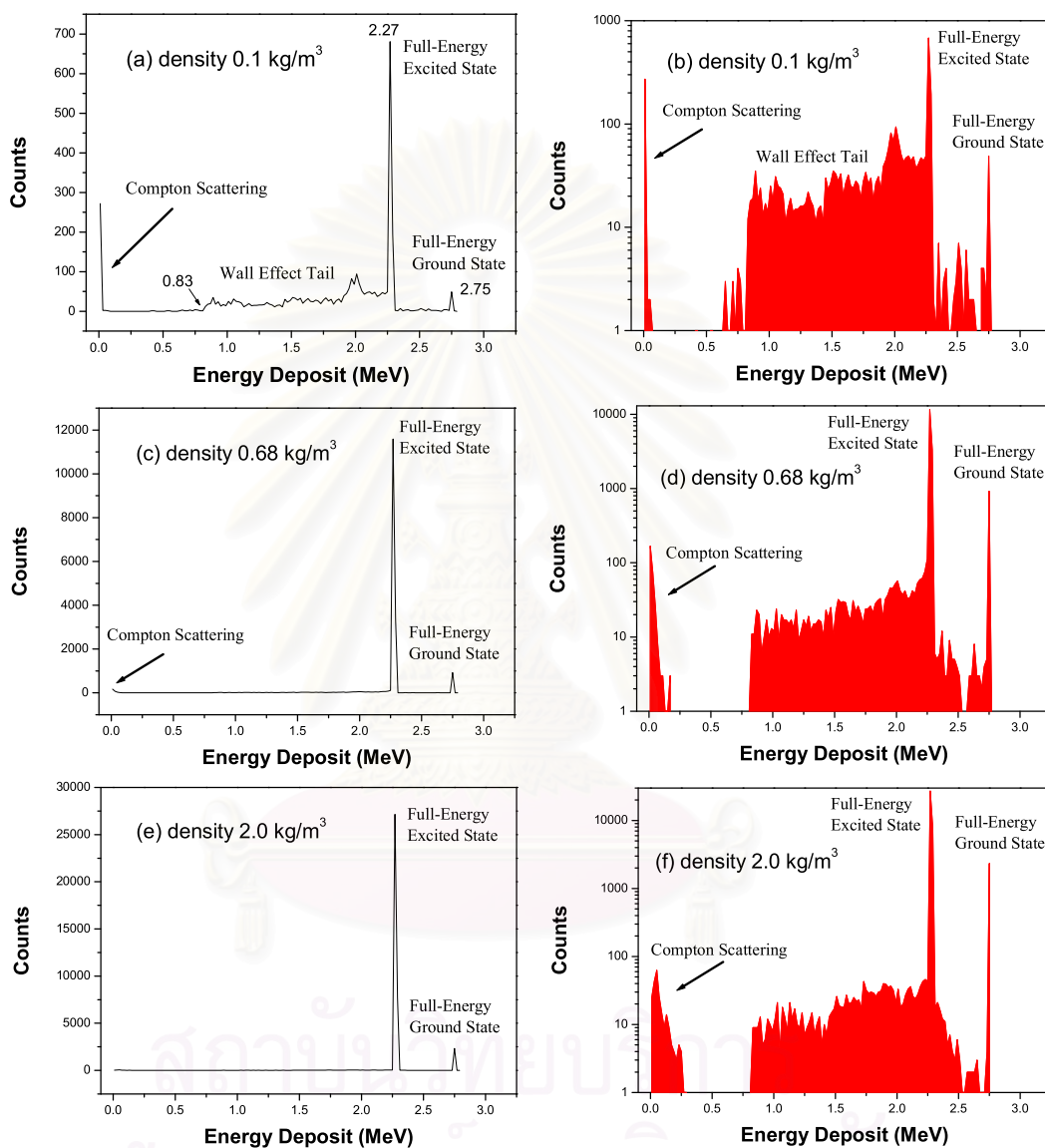


Figure 6.7: Energy distribution from a BF_3 neutron counter. Figures in the left panel display distribution in linear scale while the right panel are the same plot in logarithmic scale. The gas density in the BF_3 tube is (a,b) 0.1 kg/m^3 , (c,d) 0.68 kg/m^3 , and (e,f) 2.0 kg/m^3 . Note that the wall effect decreases while the effect from the Compton scattering expands widely. This is because of the higher grammage (or density of the medium) in the detector.

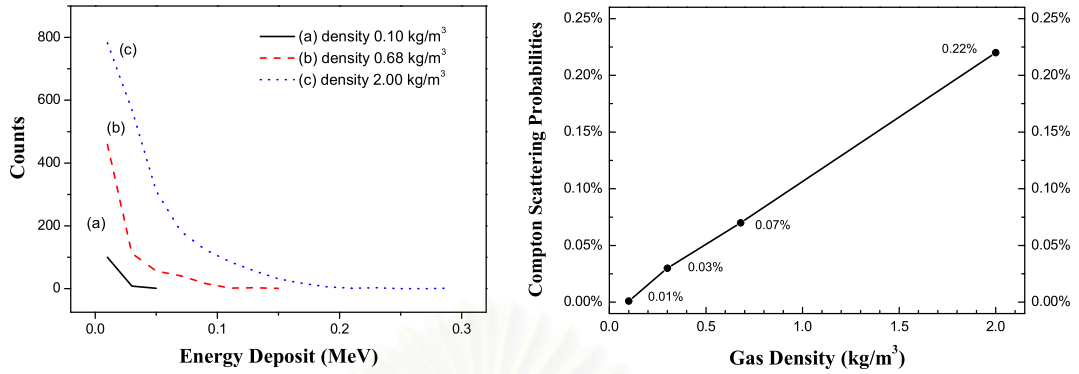


Figure 6.8: Energy deposit in the BF_3 gas chamber from electrons produced by the Compton scattering of a 0.48-MeV gamma (left), and (right) the plots of Compton scattering probabilities versus grammage. In the left panel, the BF_3 density in the gas is (a) 0.1 kg/m^3 , (b) 0.68 kg/m^3 , and (c) 2.0 kg/m^3 . The Compton scattering becomes more effective with higher grammage.

much higher peaks and small wall effect tail (which is hardly seen in linear scale). This is because the detector respond to the accumulative energy for a period of times, however there is no such gated time window set in our simulation. If the response times is low, the peak is sharp and the wall effects is small. The resolution of the detector also affects the shape of the distribution. Furthermore, the effect from the Compton scattering does not appear in the observation likes in the simulation, because its energy deposit will be accumulated with the other major pulses.

Table 6.3: Comparison between theory and simulation.

	Theory	Simulation
Full-Energy Excited State	2.31 MeV	2.27 MeV
Full-Energy Ground State	2.79 MeV	2.75 MeV
Wall Effect	0.84 MeV	0.83 MeV

In comparison between our simulation results and theory, there are a few differences as shown in Table 6.3. However, these little differences will not be taken much attention.

Simulation II: Energy distribution when shooting neutron vertically on the top of the Neutron Monitor.

From the previous simulation, we obtain the aspect of the distribution in the gas-filled detector when thermal neutrons were initiated inside the gas chamber. Next if we initiate neutron from outside of the Neutron Monitor, what aspect of the energy distribution is going to look like ? Is it the same as the previous or not?

In this simulation, various kinetic energies of a million neutrons were set shot vertically from the top surface of a 9-Tube NM64 as shown in Figure 6.9. The initial position of neutrons was set randomly with kinetic energy at (a) 0.025 eV, (b) 2 MeV, and (c) 100 MeV. The use of density parameter from calculation (0.68 kg/m^3) was applied. The results were displayed in Figure 6.10.

Discussion

This result shows the same trend as the previous simulation especially for the low-energy incoming neutrons. But at high-energy incoming neutrons, there is a small pulse beyond 3 MeV. This is due to secondary neutrons were produced locally with the increasing of incoming neutron energy and thus these secondary neutrons were captured and deposit their energies almost at the same time (millisecond). So that there is an addition of energy deposition in the detector.

Indeed, these histograms are the neutron capture reaction in the BF_3 proportional counter. No matter where neutrons come from, if they travel into the BF_3 proportional counter they may be captured by ^{10}B nucleus (which depends

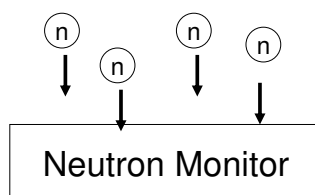


Figure 6.9: The simulation schematic. Incoming neutrons with various initial energies were shot vertically and randomly in position on the top of the Neutron Monitor.

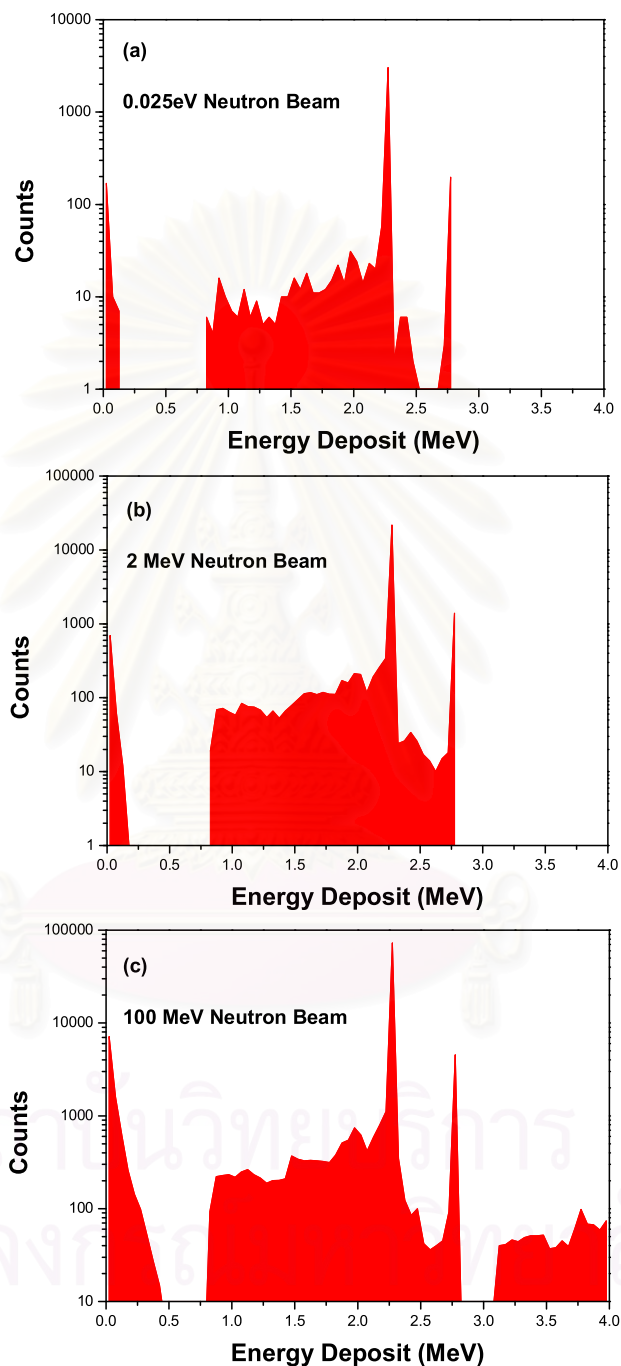


Figure 6.10: Deposited energy in the BF_3 gas chamber with density 0.68 kg/m^3 . A million neutrons were shot vertically and randomly on the top surface of the 9-Tube NM64. The initial kinetic energy of the neutron are (a) 0.025 eV, (b) 2 MeV, and (c) 100 MeV. The bin size of the histograms is 0.05 MeV/bin.

on the cross-section; it depends on many factors, such as energy and density) and produce signals as we have presented.

6.4 Counts in the Neutron Monitor

In simulations, the way to get a neutron count is by counting ${}^7\text{Li}$ ions. This is unique because a ${}^7\text{Li}$ ion is produced from a neutron capture reaction that particularly identifies the presence of neutron we want to detect.

In simulations, we shoot neutron flux on the top of the constructed geometry and we define the following quantities:

Total count

is a ratio of average neutron counts that totally occurs in the detector per incoming abundances. The total counts can be greater or less than 1 depends on number of neutrons detected in the detector.

Detection efficiency

is a parameter used to identify the efficiency of the detection of primary neutron. The detection efficiency maximizes at 1.

Total counts are different from detection efficiency. Total counts give total signals of neutrons which are captured by ${}^{10}\text{B}$ nucleus. These counts may come from primary source (we apply to the system) or reproduce from local production (mostly at lead producer). In contrast, detection efficiency is the probability of obtaining at least one a count from the detection of each incoming neutron. An example of determination of these two quantities for 5 incoming neutrons into the neutron monitor is shown in Table 6.4.

Table 6.4: An example of determination of total counts and detection efficiency for 5 incoming neutrons.

Incoming Neutron ID	Detected 2^{nd} neutrons produced from a given 1^{st} neutron	Total Counts	Detection Efficiency
1^{st}	1	16/5	4/5
2^{nd}	3		
3^{rd}	0		
4^{th}	2		
5^{th}	10		

Simulation III: Total counts and detection efficiency.

The goal for this simulation is to find the trend of the total counts and detection efficiency at various incoming neutron energies. As discussed in the previous section, the grammage affects the cross-section of the neutron capture reaction and also to the energy distribution. To get a maximum neutron count we applied the gas density parameter at 100 kg/m^3 ; we may call max density in further discussion. At such a very high grammage, the neutron absorption by boron target will always happen (more than 99.99%), so that we may ignore the effect from the grammage.

In the simulation, we initiated a flux of 10^5 neutrons on a Tube-NM64 in vertical direction. The incoming neutron energies are varied from 0.025 eV to 10 GeV. The grammage parameter 0.68 kg/m^3 was compared to 100 kg/m^3 . The results were displayed in Figure 6.11.

Discussion

From Figure 6.11, in the first graph, we find that the ratio of total counts for the use of two different grammage fluctuates between 4.8 and 5.4. Due to computer memory problem which caused the program to crash while running, the limitation of incoming neutron energy applied in the simulation cannot exceed 10 GeV.

The second graph represents the detection efficiency for two different

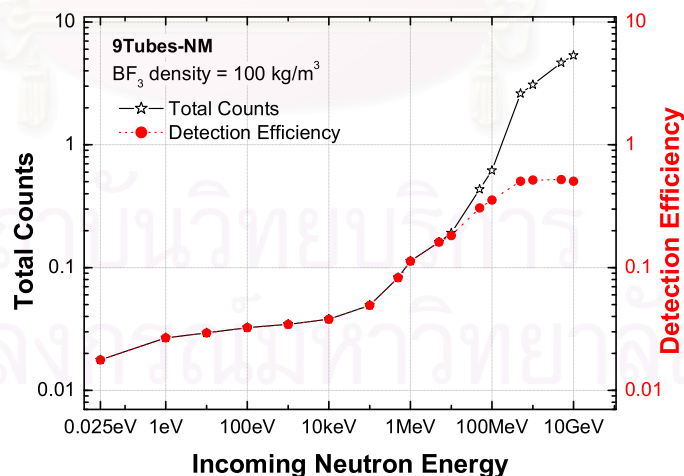
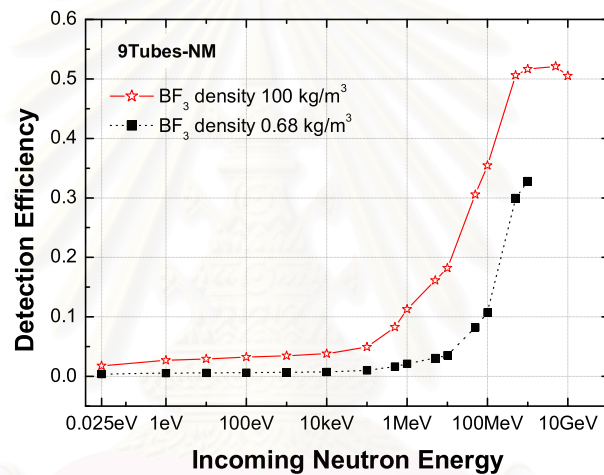
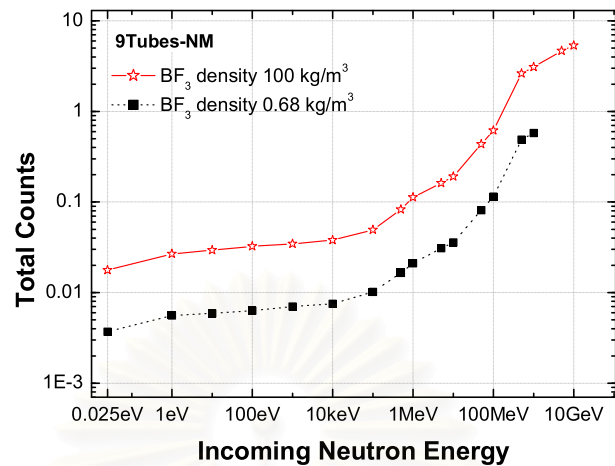


Figure 6.11: Total counts and detection efficiency. A flux of 10^5 neutrons were initiated vertically on the top of the 9Tubes-NM with various kinetic energies from 0.025 eV to 10 GeV. Note that the incident neutron beam was randomized on the top plain of the detector. The grammage parameter 0.68 kg/m^3 and 100 kg/m^3 were applied. The last graph is the comparison of the total counts and detection efficiency at grammage parameter 100 kg/m^3 .

grammages. We can see that the detection efficiency is very low until it passes the energy over 1 MeV. After 1 MeV, the counts increase rapidly. This is because the detector is designed to respond well above MeV range.

The last graph is the comparison between total counts and detection efficiency for maximum gas density. At low energy the two quantities are the same until they reach the energy around 10 MeV. At such energy, both graphs start to separate. This is because of secondary neutrons from local production start to create which increases the total counts.

Simulation IV: Random beam direction on the detector.

In the previous simulation, we initiated the incident beam on the specific location. The beam was set to arrive in the vertical direction. For the next step, we enhance the simulation by randomizing the direction of the incident beam. The inclination of the incident beam was varied uniformly from -90° to 90° with respect to the vertical direction in the vertical plane. This is analogous to the observation because, in practical, the incident neutrons from the sky come from a variety of directions.

For this simulation we compare the use of three different number of counters; which are 1, 9, and 19 counters. The results is displayed in Figure 6.12

Discussion

From the simulation, we find that the neutron counts from the random incoming direction are similar to the vertical incoming direction as in the simulation III. Furthermore, there is a different between the use of 1, 9 and 19 counters. The use of a single counter provides counts less than the use of many counters. This is because secondary neutrons produced in the detector may leave out the 1-Tube NM64 easily than using many counters.

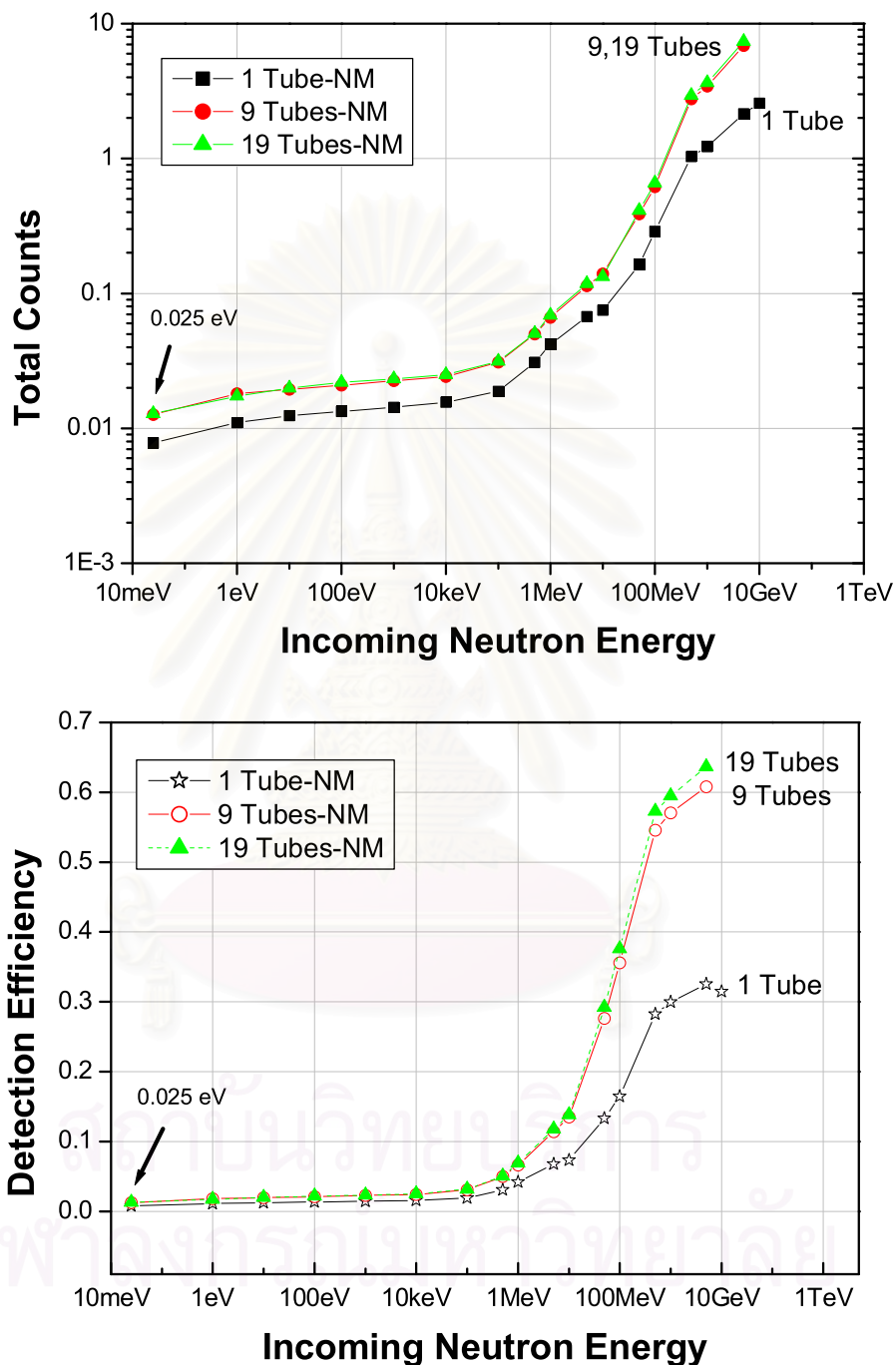


Figure 6.12: Total counts and detection efficiency from three different number of counters; 1, 9, and 19 counters. A flux of 10^5 neutrons were initiated randomly on the neutron monitor. The inclination of the incident beam were random from 0° to 180° . The use of max density parameter was applied.

Simulation V: Number of counters in the detector.

In this simulation we varied the number of counters in the detector. The goal is to investigate the neutron counts from the use of many counters in the detector compare with the use of single counter in the detector. In this simulation, the initial incoming neutron energy is varied from 0.025 eV to 10 GeV and arrive in the vertical direction. At each energy a beam of 10^5 neutrons were initiated. The result is shown in Figure 6.13. Note that the total neutron counts for each number of counter placement are shown in ratio of the use of single counter.

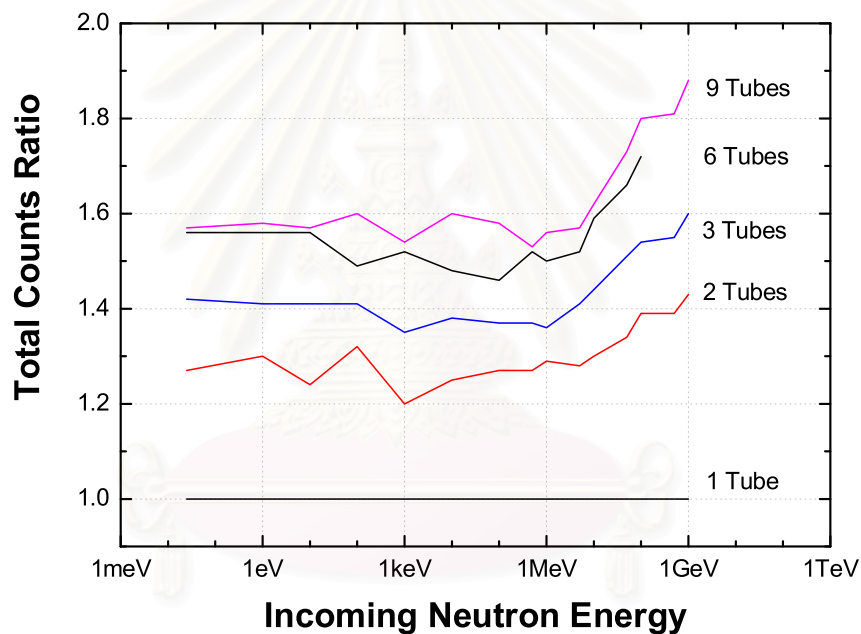


Figure 6.13: Total counts ratio for the use of 1,2,3,6, and 9 counters in the detector. The values are the ratio of counters per unit area compared with the use of a single counter. Note that the incoming neutrons were initiated in the vertical direction.

Discussion

From the simulation, we see that the total counts is minimum for the use of a single counter in the detector. The neutron counts increase with the increasing of number of counters. This is because neutrons may leave the detector easily when using one or two number of counters.

For the Princess Sirindhorn Monitor Project, the use of nine counters is

planned for each unit. The use of 9 counters placement provides a little higher response than the placement of 6 counters (which is generally used around the world).

6.5 The Lead Producer

Neutrons which interact and are captured by ^{10}B nucleus may not always directly come from the cosmic rays. In fact they can be produced locally in the material supplemented in the neutron monitor in order to increase counts. A large nucleus such as lead is preferable since the neutron production rate per unit mass of a material is roughly proportional to $A^{0.7}$ [Simpson (1949b)].

Simulation VI: Neutron interaction with lead target.

Table 6.5 presents interesting information from the simulation. In the simulation, various neutron energies (first column) were initiated at the center of a $4.5 \times 0.376 \times 2.3 \text{ m}^3$ solid lead. The second column represents the average number of collisions a neutron scatters the lead target before it leaves out the solid or loses by another process. The third column shows factor of secondary neutrons produced locally in lead target while percentages of neutron lost by inelastic scattering are displayed in the last column.

สถาบันวิทยบริการ
จุฬาลงกรณ์มหาวิทยาลัย

Table 6.5: Neutron interaction in lead at various energy.

Neutron Energy	No. of scattering	2 nd neutrons produced	Percents of absorption
1 eV	29	0	9.1%
10 eV	32	0	3.5%
100 eV	33	0	1.2%
1 keV	34	0	0.5%
10 keV	32	0	2.0%
100 keV	34	0	1.3%
1 MeV	10	0.3	31.3%
10 MeV	2	1.9	95.6%
100 MeV	3	10.9	92.2%
1 GeV	8	63.1	69.9%

Discussion

From the table, we can see that the number of collisions in the second column decreases sharply around 1 MeV compared to lower energies. This is because the cross-section for the inelastic collision becomes larger at such energy and the secondary neutron begins to produce at energy over MeV. At such high energy range, a primary neutron has high possibility to be absorbed by inelastic scattering (see fourth column), while secondary neutrons are produced increasingly (see third column).

Simulation VII: The counting rate without a lead producer.

In this simulation, we initiate a flux of 10^5 neutrons oblique to the top surface of a 9-Tube NM64. The position of the beam was randomized on the detector plane. The neutron monitor was constructed without a lead producer; the volume was replaced by vacuum in one case, and by polyethylene in the other case. This will be compared to the general geometry. The goal is to obtain the counting rate without the local production of secondary neutrons in lead target.

Discussion

From Figure 6.14, below MeV range, we find that the neutron counts (both total counts and detection efficiency) from geometry without a lead pro-

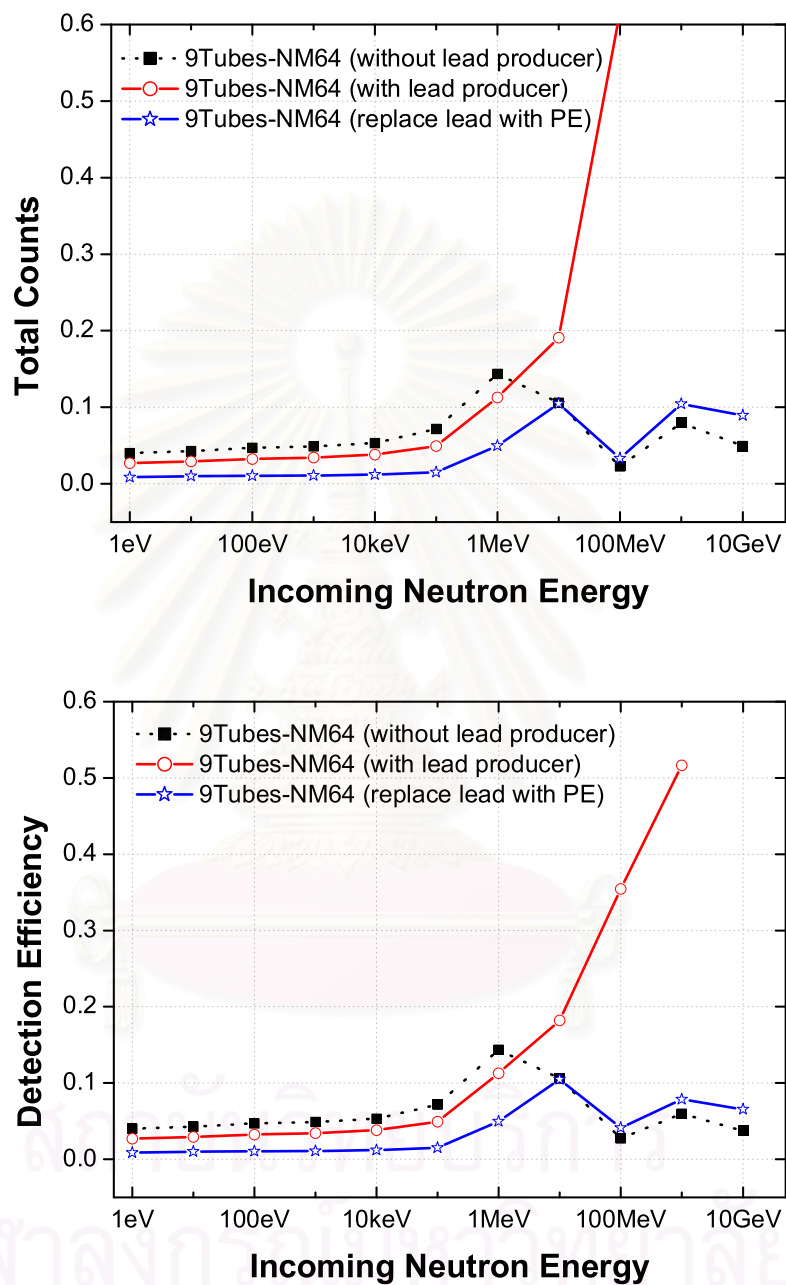


Figure 6.14: Total counts and detection efficiency, at various incoming neutron energies, from a 9-Tube NM64 without a lead producer compared with the polyethylene replacement and a general geometry using lead producer. A beam of 10^5 neutrons was initiated vertically on the random position of the top plane of the neutron monitor.

ducer inside is higher than the detection efficiency from general geometry. This is because neutrons at low energy will have many elastic scattering with lead target. In this case, the lead target acts like a reflector which may block the neutrons out before they were captured with boron nucleus. This is confirmed with the replacement of lead producer by polyethylene (dotted line with empty stars). This can imply that not having a lead target, the neutron counts may be higher because the attenuation property of the lead producer is omitted.

By the way, beyond MeV range (see Table 6.5) neutrons will have inelastic scattering with lead nucleus resulting in many secondary products including neutrons. These secondary neutrons are the reason why the neutron counts increase rapidly after this energy range. Therefore, having a lead producer is important because it helps increasing neutron counts.

6.6 The Inner Moderator

Between the counters and lead producer, there is a thick layer (0.7-1.2 inches), called inner moderator. Moderator is implemented in the neutron monitor in order to attenuate energy of the secondary neutrons produced locally at lead target before they reach the critical energy for absorption reaction to occur in the BF_3 proportional counter. The material used for the moderator are paraffin (IGY) and low density polyethylene (NM64).

The optimum thickness of the paraffin inner moderator was determined since the preliminary experiment by Simpson et al. (1953). They discovered that the count rate was found to be maximum with a thickness of 1.25 inches, being some 67% larger than the count rate without an inner moderator. In case of NM64 using low density polyethylene as the inner moderator (and also the reflector), Hatton and Carmichael (1964) have found that the optimum thickness is 0.75 inches, which provides the increase being 20% compared to the count rate without an inner moderator.

Simulation VIII: Leaving out an inner moderator.

In this simulation, the effects of the inner moderator in the neutron detection was determined. The normal geometry of the inner moderator uses low density polyethylene as the material. To leave the inner moderator out, we replaced the volume with air, so that it can be implied that the moderator thickness was set to zero ($X_{mod} = 0$).

Figure 6.15 shows the effects of having 1-inch inner moderator ($X_{mod} = 1$ inch) enclosing the BF_3 proportional counters in the 9-Tube NM64

Discussion

As displayed in Figure 6.15, at energy lower than 1 MeV, not having an inner moderator provides higher counts. This is because the moderator obstructs the arrival of neutrons into the proportional counters.

Beyond 1 MeV range, secondary neutrons begin to produce locally and now the advantage of having the inner moderator is obviously seen. It helps to facilitate neutron absorption in the proportional counter by reducing the neutron energy to the thermal endpoint.

Table 6.6: Comparison between the use of moderator thickness.

Neutron Energy	Total Counts for $X_{mod} = 0$	Total Counts for $X_{mod} = 1$ in.	Increasing Ratio [†]
1 eV	0.06	0.027	-55%
10 eV	0.065	0.029	-55%
100 eV	0.072	0.032	-55%
1 keV	0.077	0.034	-55%
10 keV	0.079	0.038	-52%
100 keV	0.101	0.047	-51%
1 MeV	0.151	0.113	-25%
10 MeV	0.164	0.191	17%
100 MeV	0.478	0.616	26%
1 GeV	2.804	3.083	10%
10 GeV	4.44	5.336	20%

[†] Remark: The negative sign represents the decreasing ratio.

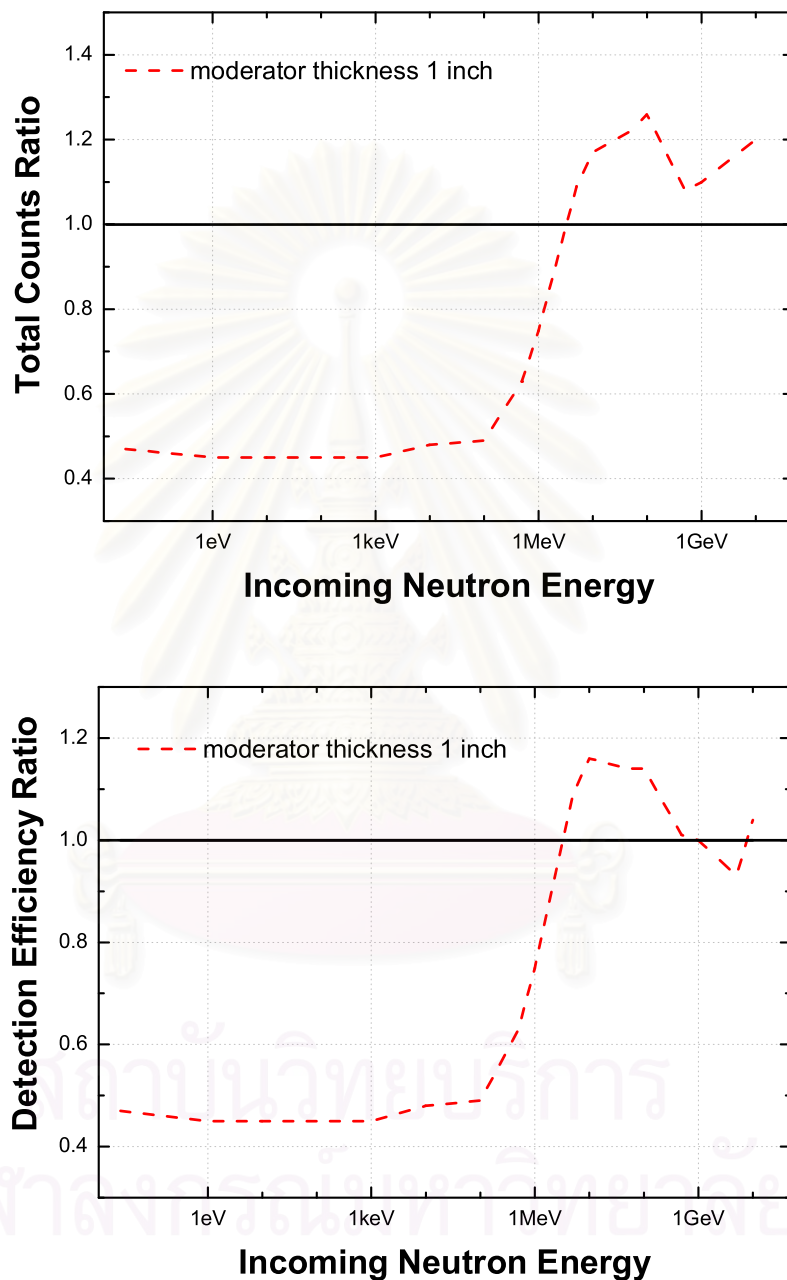


Figure 6.15: Total counts ratio and detection efficiency ratio at various incoming neutron energies between the geometry with moderator implemented and the geometry without moderator. Note that 10^4 neutrons for each incoming energy (varies from 0.025 eV to 10 GeV) were initiated vertically on the neutron monitor.

Table 6.6 shows the comparison of total neutron counts from the 9-Tube NM64 without inner moderator and having 1-inch inner moderator. The increasing ratio was displayed in the last column. This is difficult to compare with experimental result by Hatton and Carmichael (1964); the increasing is 20% for the optimum thickness at 0.75 inches, because their results include all energy range, which in reality the neutron spectrum is inversely proportional to energy as shown in Figure 2.7.

Although this simulation did not determine the optimum thickness for inner moderator, but its function has been justified.

Some difficulties when using GEANT4 simulate the neutron moderation process.

As discussed in section 3.3: Neutron Attenuation, that a neutron undergoes elastic scattering with a target proton nucleus and the recoil neutron have a reduced energy. From the theory, we approximate that the target is at rest without kinetic energy, and we estimate that the number of collisions for a 2-MeV neutron to reduce its energy to thermal energy is 18 on average. In fact, the target proton is not at rest. This will not have an important effect for the incoming fast neutrons. In case of slow neutrons, this effect becomes more significant since neutron may gain energy from the target.

In the simulation, if we set the temperature of the moderator to room temperature (298 K) the number of collisions to thermalize a 2-MeV neutron is varied between 25 to 50. Furthermore, we change the temperature to 3 K. We find that the number reduces to the value between 20 to 30.

6.7 The Reflector

The reflector is designed to enclose the detector. Its function is to reflect unwanted background neutrons, which have been produced in the environment,

and to allow high energy atmospheric neutrons to enter the detector.

The optimum thickness for the reflector had been determined by Hatton and Carmichael (1964). Their results indicate that the counting rate is a maximum at a reflector thickness about 2 inches. From the point of view of the reflecting neutrons produced within the monitor, a reflector thickness about 2 inches is quite adequate. This is in agreement with theoretical considerations [Hatton (1971)], because the diffusion length of thermal neutrons in polyethylene is 2.4 cm and a negligible number of neutrons thermalised beyond 2 inches in the reflector will diffuse back to the counters (~ 3 diffusion lengths).

Simulation IX: Reflection of the neutrons on the reflector.

In this simulation we investigated the reflection property of the reflector using low density polyethylene as the material. A 3-inch thickness of reflector is used as the test object for various incoming neutron energies. The result is shown in Figure 6.16.

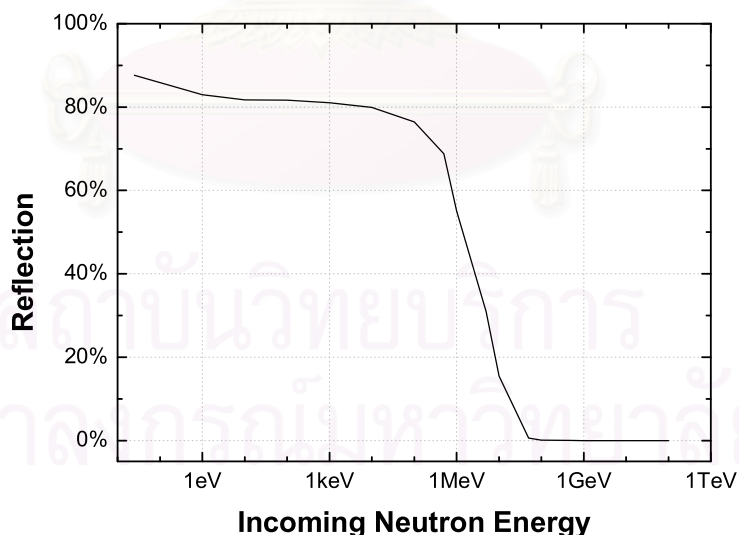


Figure 6.16: Percentages of reflecting neutrons from the reflector with a thickness of 3 inches.

Discussion

From the simulation, Figure 6.16 shows the percentages of reflecting neutrons from the reflector using low density polyethylene with a thickness of 3

inches. We found that neutrons at low energy are mostly rejected by the reflector. The penetration of neutrons through the reflector increases rapidly around 1 MeV and maximizes around 50 MeV with full penetration.

In case of the neutron monitor, the low energy neutrons (below 100 keV) will mostly be rejected by the reflector. The major incoming neutrons in the detector will have energy higher than 1 MeV. These neutrons are the target for the detection since they were produced by the cosmic rays in the atmosphere.

6.8 Effects from Environments

Environments, i.e. humidity, rain, snow, and ice, may sometimes have effects to the neutron counts. They may obstruct the arrival of neutrons in the detectors. On the other hand, they help increasing counts by reflecting neutrons into the detectors as shown in Figure 6.17.

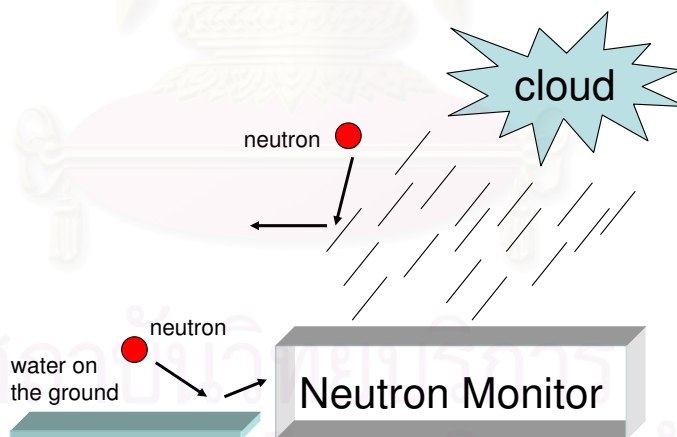


Figure 6.17: Neutron reflection from surroundings. Neutrons are reflected by molecules of the water during the rain, and flooding water on the ground (from rain or other causes) can reflect neutrons into the detector.

Simulation X: Neutron reflection from water on the ground

In this simulation, we determined the reflection of neutrons from flooding water on the ground into the neutron monitor. In this situation, there was some

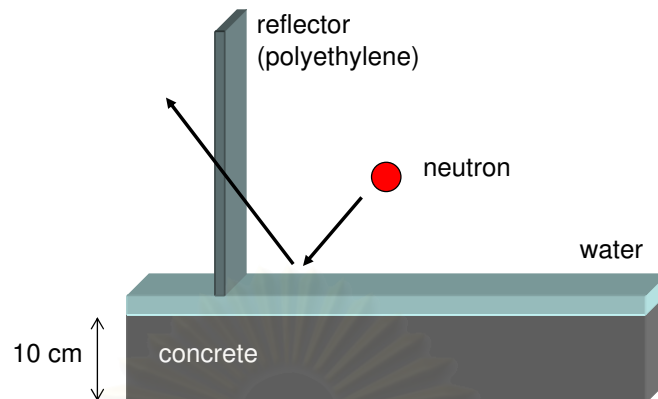


Figure 6.18: Simulation schematic. Neutrons were initiated obliquely with the angle 45° on the water. The reflector made of low density polyethylene with a thickness of 3 inches are placed at the distance of 22 cm from the position of the incident neutrons. Note that the height of the water and the concrete were set to 1 cm and 10 cm, respectively.

water lying at 1 cm high on a concrete with a thickness of 10 cm and neutrons were initiated obliquely with the angle 45° on the water, as shown in Figure 6.18. Some of reflected neutrons travel to the neutron monitor, but a small abundances can penetrate the reflector. The results are presented in Figure 6.19

Discussion

From the simulation result in Figure 6.19, we found that water and concrete can reflect some of neutrons to the neutron monitor. In case of not having a concrete beneath the water, most of reflection (maximum at 15% of incoming abundances) occurs from the incident of low energy neutrons under 10 keV. The reflection decreases rapidly after 10 keV, and at 1 MeV the reflection decreases to 5% of incoming abundances.

The ratio of neutrons penetrating the reflector into the neutron monitor is shown in the dotted line. Only 2% of incoming abundances (at energy below MeV) can pass through the reflector. This 2% may increase a little neutrons counts at energy below MeV. Above MeV, the reflected neutrons are rare since the water behaves as the reflector for the incoming neutron at low energy.

In case of having only a concrete, the results are in opposite as we ex-

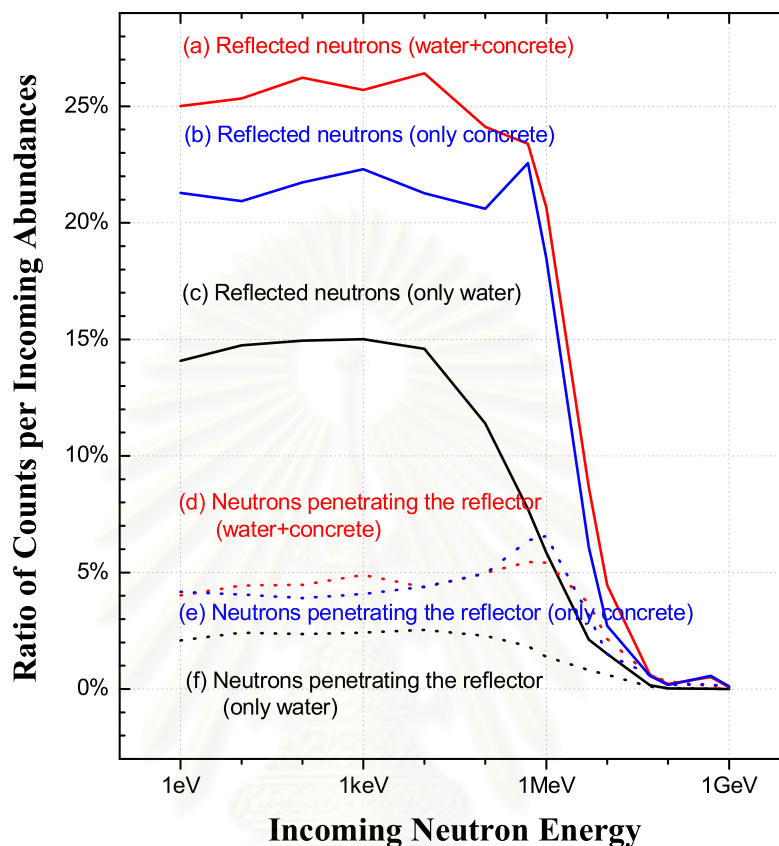


Figure 6.19: Reflected neutrons from the ground to the reflector (solid line), and which is traveling through the reflector (dotted line). The black lines (c and f) are from the consideration of having only water, and the blue lines (b and e) are from the case of having only concrete, and the red lines (a and d) are from the case of having water above the concrete.

pected. We expected that the concrete might absorb neutrons whereas the simulation shows that the concrete also reflects neutrons into the detector. The situation of having a 10 cm of concrete thickness increases penetration of neutrons into the neutron monitor from about 2% to about 5%.

6.9 Contribution from Other Charged Particles to the Neutron Monitor

As discussed in the Chapter 2, atmospheric cosmic rays contain several species of particles. These particles are generated by multiple inelastic collisions

of primary incident particles with atomic gas. In case of the arrival of the cosmic rays into the detector, if the particles have sufficiently high kinetic energy, they may collide with materials in the detector and generate a cascade of secondary products.

In case of the neutron monitor, the material is a lead producer. At the lead producer, variety of secondary products are produced, such as pions, muons, neutrons, protons, and electrons. The local production requires appropriate range of kinetic energy which are different for each arriving particles.

Since the purpose of setting the neutron monitor is to count cosmic ray secondary neutrons at ground level. In fact, the observed counts from the neutron monitor may not come from the arrival of neutrons only. It could come from other kinds of particles which induce counts by neutron production at the lead producer. The simulation results for six different particle species arriving at NM-64 in vertical direction is displayed in Figure 6.20. This simulation was done by Clem (1999) using FLUKA combined with his program.

As resulted from Figure 6.20, detector response is optimized to measure the hadronic component of ground level secondaries. In case of leptons, the neutron monitor response to muons above 1 GeV is roughly 3.5 orders of magnitude less than the hadrons. At such energy region, the primary mechanisms for muon induced counts are neutron production in photo-nuclear interactions and electromagnetic showers resulting in multiple ionization tracks in a counter. Below 1 GeV, muons lose energy by ionization loss in the detector and then only stopping negative charge muons are captured by a lead nucleus into a mesic orbit and are absorbed by the nucleus. The de-excitation of the nucleus occurs with the emission neutron which is reflected in increasing of count with decreasing energy. One of the possible μ^- capture reactions is



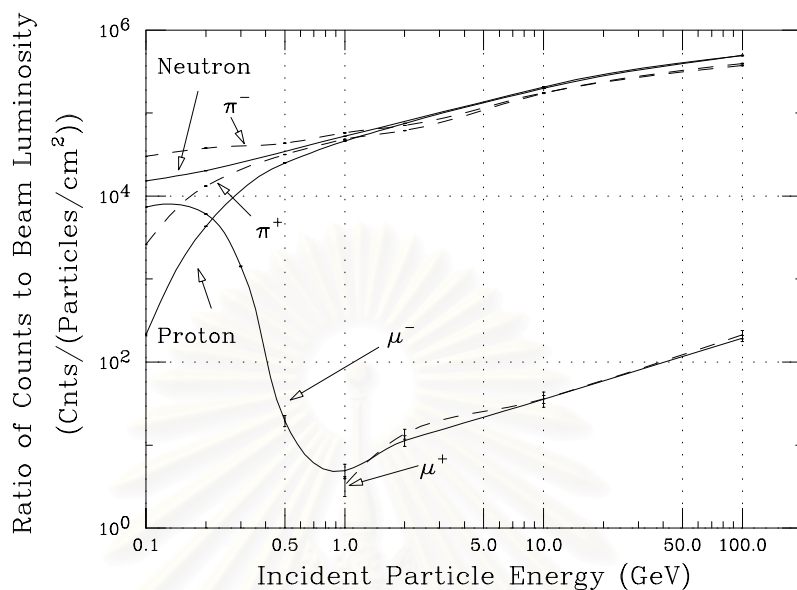


Figure 6.20: Detection efficiency of a NM-64 with $^{10}\text{BF}_3$ counters for 6 different particle species arriving in the vertical incident direction. This result was determined using FLUKA combined with programs written by Clem. [Clem et al. (2000)]

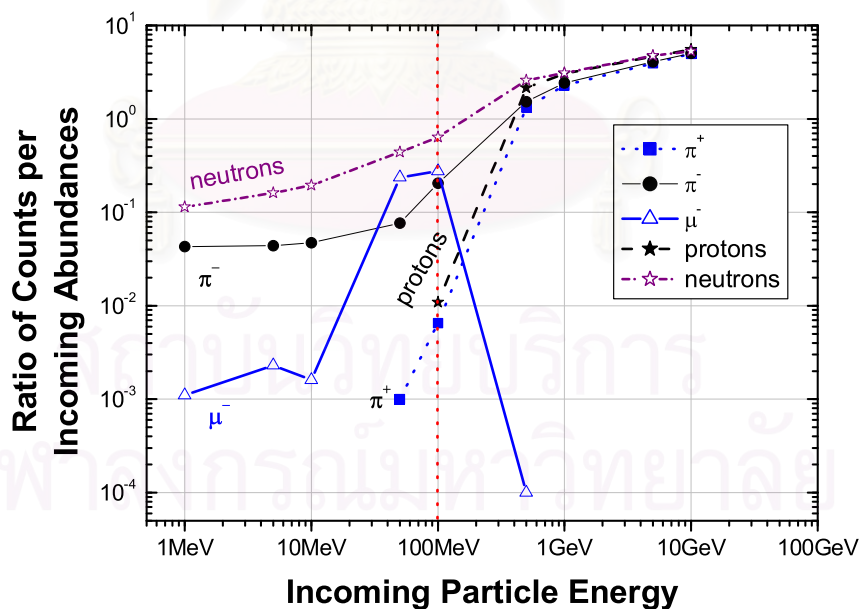


Figure 6.21: Ratio of counts per incoming abundances in a 9-Tube NM64 from the arrival of six different species of particles; π^+ , π^- , μ^+ , μ^- , p, and n. Note that the simulation gives zero count for the incoming of μ^+ for an entire range of energy, so that there is no data for μ^+ in the graph.

The bound state occurs in a short period of times. Positive charge muons does not form into mesic orbit since there is a repulsive from Coulomb barrier between the positive charge muon and the target nucleus.

In case of neutrons and protons, there is no difference in their response in high energy region, while at lower energies the ionization energy loss of protons becomes significant, greatly reducing the probability of an interaction, which reflects in the decreasing count.

Positive and negative charge pions produce almost identical responses at high energies, while at energies lower than 1 GeV, pion minus undergoes nuclear capture like muon minus.

Simulation XI: Counts from other incident particles.

In the simulation we initiate six different species of particle; neutrons, protons, pions (negatively and positively charged), and muon (negatively and positively charged), in the vertical direction. The number of events for each particle type are 10,000 events. The kinetic energy of the arriving particle varies from 1 MeV to 10 GeV. The results are displayed in Figure 6.21.

Discussion

This result provides a similar consistence with the result from Clem et al. (2000) in Figure 6.20. However, there are some differences. Since the precompiled library we used in the GEANT4 simulation did not include deep inelastic scattering for the positive and negative charge muons, there is a disappearance of neutron counts for arriving muons beyond 0.5 GeV. Below such energy, the ionization energies loss of muons becomes significant, greatly reducing their energy to zero. Stopping μ^- is captured and then neutron production is induced at lead target.

In general, the μ^- capture reaction can occur in several channels. The neutron emission channel is more preferable for high atomic number nuclear target

such as lead. At lower energy, muons will have high probability to stop at the reflector which results in the decreasing of counts from neutron production.

In case of pions, stopping negative pions undergo nuclear captured like negative muons. In addition, negative charge pions may decay into antimuon neutrinos and negative charge muons. These negative charge muons may also produce neutron counts as mentioned before. For positive charge pions, the decays result in muon neutrinos and positive charge muons, which provide no neutron count at all.

Our simulation results and Clem et al. (2000) reveal to us that the counts from the neutron monitor may not particularly come from the atmospheric neutron arriving into the detector. It includes the effects from the arrival of other energetic particles. In fact, the purpose of setting up the neutron monitor is to detect the abundance of cosmic rays at period of times and neutrons counts are the key to such the quantity.



สถาบันวิทยบริการ
จุฬาลงกรณ์มหาวิทยาลัย

Chapter 7

Conclusions

The simulation using GEANT4 program provides energy distributions in the proportional counters, which is used to identify the presence of the neutrons in the detector. This result is in agreement with the preliminary observations and theoretical considerations. The simulations provided sharper peaks and effects from the electron-photon Compton scattering. This is different from the measurements since the resolution and response times of the detectors and multiplicities need to be taken into account in the simulations.

The neutron counts at various energies of incoming neutrons have been determined. We obtained the total counts and detection efficiency in the simulations. The total counts give the definition of entire neutron counts in ratio of the incoming abundances while detection efficiency is referred to efficiency of the neutron monitor to respond for the incoming neutrons in ratio of the incoming abundances. The neutron counts increase with the increasing of incoming energy since the neutron production increases with the increasing incoming neutron energy. Moreover, the neutron counts have been determined for the variation of number of counters implemented in each unit. The vertical direction and the inclined direction of the arriving neutron are also determined.

The functions of the major components (the lead producer, the inner moderator, and the reflector) were also determined by the simulations. The lead producer is used to increase counts by producing many secondary neutrons inside the detector. From the simulation, we found that its function responds for the energy of incoming neutron higher than ~ 1 MeV.

The inner moderator is used to moderate neutrons from local productions before they undergo nuclear absorptions in gas-filled chambers. From the simulation, we found that it has an advantage at incoming neutron energy beyond

~ 1 MeV. For energy less than ~ 1 MeV, it obstructs the arrivals of neutrons into the gas-filled chambers resulting in the less neutron counts compared with not having the inner moderator.

The reflector has a function of reflecting unwanted background neutron produced in environments, and to allow high energy atmospheric neutron into the detector. Its functions have been determined by the simulation, and found that it can reflect mostly ($\sim 80\%$) 1 eV to 100 keV neutrons and allow above MeV neutron into the detector. The results show that the neutron monitors were designed to respond well for the incoming of atmospheric neutrons at high-energy.

Furthermore, the effects from scattered neutron from water on the ground into the detector have been determined. The simulation for a particular event shows that a small fraction of neutrons (less than 5%) below MeV have been scattered into the detector.

Finally, the simulations using GEANT4 program also show the contribution of incoming charged particles resulting in the neutron counts.

References

- Allkofer, O. C. and Grieder, P. K.**, “Physics Data: Cosmic Rays on Earth”, Fachinformationszentrum Energie, Physik, Mathematik GmbH, Karlsruhe, Germany (1984).
- Arny, T. T.**, “Explorations: Stars, Galaxies, and Planets”, Updated version (2003).
- Bartol Research Institute Neutron Monitor Program:**
<http://www.bartol.udel.edu/~neutronm>.
- Carmichael, H.**, “Cosmic Rays”, IQSY Instruction Manual No. 7, London: IQSY Secretariat (1964).
- CERN Web Site:** <http://www.cern.ch>.
- Clem, J.**, “Atmospheric Yield Functions and Response to Secondary Particles of Neutron Monitors”, Proceeding in the 26th International Cosmic Rays Conference, Salt Lake City, **7**, 317-320 (1999).
- Clem, J. et al.**, “Neutron Monitor Response Functions”, Space Science Reviews, **93**, 335-359 (2000).
- Clem, J.**, “Neutron Monitor Detection Efficiency”, unpublished presentation document in 2004 Annual CRONUS Collaboration Meeting (2004).
- Fowler, I. L.**, “Very Large Boron Trifluoride Proportional Counters”, Review of Scientific Instruments, **34**, Issue 7, 731-739 (1963).
- Friedlander, M. W.**, “Cosmic Rays”, Harvard University Press (1989).
- GEANT4 Home Page:** <http://geant4.web.cern.ch/geant4>.

- Hatton, C. J. and Carmichael, H.**, “Experimental Investigation of the NM-64 Neutron Monitor”, Canadian Journal Phys., **42**, 2443-2472 (1964).
- Hatton, C. J.**, “The Neutron Monitor”, Progress in Elementary Particle and Cosmic Ray Physics, **10**, 1 (1971).
- Hewitt, J. et al.**, “Ames Collaborative Study of Cosmic Ray Neutrons: Mid-Latitude Flights”, Health Physics, **34**, 375 (1978).
- Kaplan, I.**, “Nuclear Physics”, Addison-Wesley (1955), Chapter 18: Neutron Physics.
- Krane, K. S.**, “Introductory Nuclear Physics”, John Wiley & Son (1988), Chapter 12: Neutron Physics.
- Lang, K. R.**, “The Cambridge Encyclopedia of the Sun”, 1st ed., (2001).
- Lilley, J.**, “Nuclear Physics-Principles and Applications”, John Wiley & Son (2001), Chapter 5.5: Neutron Moderation.
- Merker, M. et al.**, “Time Dependent Worldwide Distribution of Atmospheric Neutrons and of Their Products Part 1”, J. Geophys. Res., **78**, 2727 (1973).
- Normand, E. and Baker, T.J.**, “Altitude and Latitude Variations in Avionics SEU and Atmospheric Neutron Flux”, IEEE Trans. Nucl. Sci., **40**, 1484 (1993).
- Normand, E.**, “Single Event Effects in Avionics”, IEEE Trans. Nucl. Sci., **43**, 461 (1996).
- Rose, D.C. et al.**, “Latitude Effect of the Cosmic Ray Nucleon and Meson Components at Sea Level from the Arctic to the Antarctic”, Canadian Journal Phys., **34**, 968 (1956).

Simpson, J. A., “The Latitude Dependence of Neutron Densities in the Atmosphere as a Function of Altitude”, Phys. Rev., **73**, 1389 (1948).

Simpson, J. A., “On the Latitude Dependence of Neutrons and Low-Energy Nuclear Disintegrations”, Proceeding of the Echo Lake Cosmic Ray Symposium, Department of the Navy, Washington, D.C., 175-180 (November 1949).

Simpson, J. A., “On the Production of Neutrons and Its Relationship to the Primary Cosmic Rays”, Proceeding of the Echo Lake Cosmic Ray Symposium, Department of the Navy, Washington, D.C., 252-254 (November 1949).

Simpson, J. A., Fonger, W.H. and Treiman, S.B., “Cosmic Radiation Intensity-Time Variations and Their Origin: 1. Neutron Intensity Variation Method and Meteorological Factors”, Phys. Rev., **90**, 934 (1953).

Simpson, J. A., “Cosmic Radiation Neutron Intensity Monitor”, Annals of the International Geophysical Year, Parts VII, Pergamon Press, London (1957).

Space Physics Data System, Climax and Haleakala Neutron Monitor Datasets: <http://ulysses.sr.unh.edu/NeutronMonitor>.

Space Weather Canada: <http://www.spaceweather.gc.ca>.

Taber, A. and Normand, E., “Single Event Upset in Avionics”, IEEE Trans. Nucl. Sci., **40**, 120 (1993).

Taber, A. and Normand, E., “Investigation and Characterization of SEU Effects and Hardening Strategies in Avionics”, DNA-Report DNA-TR-94-123, Defense Nuclear Agency (Feb 1995).

Thai Space Weather: <http://www.thaispaceweather.com>.

Appendix

Codes and Environments

In our work the codes we used for simulations were modified from the “*GEANT4’s Novice Example*”. There are many files stored in the main directory and 2 sub-directories. The important components in the main directory are

- **GNUmakefile**

This is the make file, used to link libraries with the main program. It assigns the destination of the output.

- **main.cc**

This is the main program. In this file the source files needed to be implemented are declared and those files are stored in `/src` and `/include`.

- **/src**

Stores source files (`.cc` extension). Its header of each file is stored in directory `/include`.

- **/include**

Stores the header files (`.hh` extension).

In the sub-directory `/src` and `/include`, there are 11 classes (with their header files) needed to link with the main program (`main.cc`), which are

- **EventAction**

The trajectory setup for the visualization mode.

- **ExN01PrimaryGeneratorAction**

The kinematic setup.

- **ExN02TrackerHit**
Manages the hit record in the volume.
- **ExN02TrackerSD**
Manages the hit record in the volume.
- **ExN07Run**
Manages the record setup in each run.
- **ExN07RunAction**
Manages the verbose setup in each run.
- **Neutron_Monitor**
The neutron monitor geometry.
- **SteppingAction**
Manipulates the track ID, particle types, and physics processes in each track.
- **SteppingVerbose**
The verbose setup.
- **T01StackingAction**
This class is used to classify the particle tracks in each event.
- **VisManager**
This class is the environment setup in the visualization mode.

All file is supplemented in the CD-ROM implemented at the back cover of the thesis.

Curriculum Vitae

Mr. Kanin Aungskunsiri was born in October 31, 1980 in Phuket. He received his bachelor degree of science in physics from *Chulalongkorn University* in 2001. During his thesis study, he was supported financially by the Basic Research Grant from *the Chulalongkorn University Research Unit* and *the Thailand Research Fund*.

Conference Presentations:

- 2005 **Kanin Aungskunsiri, Burin Asavapibhop and David Ruffolo**, “The Princess Sirindhorn Neutron Monitor Simulation”, *The 9th Annual National Symposium on Computational Science and Engineering (ANSCSE9)*, Faculty of Science, Mahidol University (March 23-25, 2005).

สถาบันวิทยบริการ
จุฬาลงกรณ์มหาวิทยาลัย